HHS Public Access

Author manuscript

Acta Biomater. Author manuscript; available in PMC 2018 March 28.

Published in final edited form as:

Acta Biomater. 2017 January 15; 48: 499–520. doi:10.1016/j.actbio.2016.10.020.

Cytocompatibility and early inflammatory response of human endothelial cells in direct culture with Mg-Zn-Sr alloys

Aaron F. Cipriano[a,b], **Amy Sallee**[a], **Myla Tayoba**[a], **Mayra C. Cortez Alcaraz**[a], **Alan Lin**[a], **Ren-Guo Guan**[c], **Zhan-Yong Zhao**[c], and **Huinan Liu**[a,b,d,e,*]

[a]Department of Bioengineering, University of California, Riverside, CA 92521, USA

[b]Materials Science & Engineering Program, University of California, Riverside, CA 92521, USA

[c]School of Materials and Metallurgy, Northeastern University, Shenyang 110004, China

[d]Stem Cell Center, University of California, Riverside, CA 92521, USA

[e]Cell, Molecular and Developmental Biology Program, University of California, Riverside, CA 92521, USA

Abstract

Crystalline Mg-Zinc (Zn)-Strontium (Sr) ternary alloys consist of elements naturally present in the human body and provide attractive mechanical and biodegradable properties for a variety of biomedical applications. The first objective of this study was to investigate the degradation and cytocompatibility of four Mg-4Zn-xSr alloys (x = 0.15, 0.5, 1.0, 1.5 wt%; designated as ZSr41A, B, C, and D respectively) in the direct culture with human umbilical vein endothelial cells (HUVEC) *in vitro*. The second objective was to investigate, for the first time, the early-stage inflammatory response in cultured HUVECs as indicated by the induction of vascular cellular adhesion molecule-1 (VCAM-1). The results showed that the 24-h *in vitro* degradation of the ZSr41 alloys containing a β-phase with a Zn/Sr at% ratio ~1.5 was significantly faster than the ZSr41 alloys with Zn/Sr at% ~1. Additionally, the adhesion density of HUVECs in the direct culture but not in direct contact with the ZSr41 alloys for up to 24 h was not adversely affected by the degradation of the alloys. Importantly, neither culture media supplemented with up to 27.6 mM Mg^{2+} ions nor media intentionally adjusted up to alkaline pH 9 induced any detectable adverse effects on HUVEC responses. In contrast, the significantly higher, yet non-cytotoxic, Zn^{2+} ion concentration from the degradation of ZSr41D alloy was likely the cause for the initially higher VCAM-1 expression on cultured HUVECs. Lastly, analysis of the HUVEC-ZSr41 interface showed near-complete absence of cell adhesion directly on the sample surface, most likely caused by either a high local alkalinity, change in surface topography, and/or surface composition. The *direct* culture method used in this study was proposed as a valuable tool for studying the design aspects of Zn-containing Mg-based biomaterials *in vitro*, in order to engineer solutions to address current shortcomings of Mg alloys for vascular device applications.

*Corresponding author at: Department of Bioengineering, University of California at Riverside, 900 University Avenue, Riverside, CA 92521, USA., huinan.liu@ucr.edu (H. Liu).

Keywords

Biodegradable Magnesium Zinc Strontium alloy; Mg-Zn-Sr alloy; Human umbilical vein endothelial cells (HUVEC); Induction of vascular cell adhesion molecule-1 (VCAM-1); Early *inflammatory response*; Biomedical implants

1. Introduction

Magnesium (Mg) alloys specifically designed for biodegradable implant applications have been the focus of biomedical research since the early 2000s [1–3]. Physicochemical properties of Mg alloys make these metallic biomaterials excellent candidates for temporary biodegradable implants in orthopedic and cardiovascular applications [1–4]. Most notable is the fact that the human body contains a large amount of Mg ions and can effectively metabolize the degradation products of Mg [1–3]. Therefore, temporary biodegradable metallic implants are idealized to be superior alternatives to permanent implants in that they would eliminate the need for implant removal surgeries following healing of the damaged tissue. By doing so, Mg-based biodegradable implants could reduce the burden on the healthcare system by mitigating risks and costs [5,6]. Furthermore, as Mg alloys continue to be investigated for biomedical applications, it is necessary to understand whether Mg-based materials or the alloying elements have the intrinsic ability to direct an immune response to improve implant integration while avoiding cell-biomaterial interactions leading to chronic inflammation and/or foreign body reactions [7,8]. In contrast, previous studies have shown that conventional permanent metallic implants, and associated wear debris, can trigger chronic inflammatory responses, result in tissue loss, and are prone to infection [1,6,9].

In general, the initial (acute) inflammatory response (i.e. innate immunity) to biomaterials is activated by the reaction of vascularized connective tissue to injury caused either by trauma or implantation [10,11]. The physiological response of inflammation consists of a complex series of meticulously controlled responses which cannot possibly be summarized in a few sentences; however, the informed reader is referred to excellent reviews on the inflammatory response to biomaterials [8,11]. Endothelial cells (EC) play an important role in the regulation of immune and inflammatory local responses by expressing, among other things, cell adhesion molecules (CAM) [12,13]. CAM expression in activated ECs (type II activation) can be induced by pro-inflammatory cytokines, e.g. tumor necrosis factor α (TNFα) [12,13], released by inflammatory cells activated on contact with adsorbed proteins on the implanted biomaterial [8,11,14]. In turn, these adhesion molecules help recruit leukocytes from circulating blood and facilitate transendothelial migration to the site of injury to initiate the acute inflammatory response [8,11–14]. Additionally, previous *in vitro* studies showed that CAM expression in ECs was activated by elevated concentrations of metallic ions typically found in permanent metallic implants [7,15–23]. Vascular cell adhesion molecule-1 (VCAM-1) is an immunoglobulin superfamily-specific receptor that provides high-affinity interactions between ECs and integrins on the leukocyte surface and facilitates transendothelial migration [10,13,14]. Moreover, VCAM-1 binds with monocytes, but not neutrophils, and it is the first CAM expressed in chronic inflammation such as atherosclerosis (before atherosclerotic plaque development) [13,14,24] and restenosis

following coronary stent implantation [25]. Thus, VCAM-1 can be used as an indicator of *in vitro* EC activation during the early stages of inflammation. Furthermore, previous studies supported the applicability of human umbilical vein endothelial cells (HUVEC) to model and investigate components of the inflammatory response, such as CAM expression [7,17].

Previously, we reported the development of Mg-Zinc-Strontium (Mg-Zn-Sr) ternary alloys and the evaluation of their biological performance for biomedical applications [26–28]. Furthermore, we reported the *in vitro* direct culture method to mimic *in vivo* physiological conditions and evaluate cell responses at the cell-biomaterial interface (*direct contact*) and on the culture plate (*indirect contact*; exposure to solubilized degradation products) surrounding the Mg-based biomaterial [29]. The direct culture method was introduced to provide a more comprehensive *in vitro* method, as compared with ISO 10993-based methods, for the initial rapid screening of cytocompatibility and degradation of Mg-based biomaterials [29]. The direct culture method was introduced as part of a field-wide effort to improve and standardize the *in vitro* testing of Mg-based biomaterials [29–32]. Thus, the first objective of this study was to investigate the degradation and cytocompatibility of four Mg-4Zn-xSr alloys (x = 0.15, 0.5, 1.0, 1.5 wt%; designated as ZSr41A, B, C, and D respectively) in the direct culture with HUVECs *in vitro*. The second objective was to investigate the induction of an inflammatory response in HUVECs as indicated by the expression of VCAM-1 activated by the degradation products of the ZSr41 alloys. While several recent *in vivo* studies reported adequate immunological response during the foreign body reaction or fibrosis stages following implantation of Mg-based materials [33–37], sparse literature is found on the early-stage inflammatory response. Specifically, to the authors' knowledge, early-stage inflammatory induction by the degradation of Mg-based materials has only been investigated *in vitro* with primary murine and human macrophages [38] and with dendritic cells [39]. In both cases, the Mg-based materials and the respective degradation products were not found to have detrimental immunomodulatory effects. This study reported for the first time on the *in vitro* transient inflammatory activation of ECs induced by the degradation products of Zn-containing Mg alloys.

2. Materials and methods

2.1. Preparation of ZSr41 alloys, Mg control, and reference materials

The ZSr41 alloys in this study had a nominal composition of 4 wt% Zn with 0.15, 0.5, 1.0, or 1.5 wt% Sr; these alloys were designated as ZSr41A, ZSr41B, ZSr41C, and ZSr41D accordingly with increasing Sr content. Details pertaining to the metallurgical process and heat treatment used for alloy preparation are described elsewhere [26,27]. The heat-treated 1.0 mm thick sheets of ZSr41 alloys were cut into 5 × 5 mm squares. Likewise, commercially pure Mg sheets (99.9%, As-rolled, 1.0 mm thick, Cat# 40604; Alfa Aesar, Ward Hill, MA, USA) were cut into 5 × 5 mm squares and used as a control in this study. Commercially available AZ31 (1.0 mm thick, Cat# 44009; Alfa Aesar) and Nitinol (NiTi; 0.25 mm thick, Cat# 44953; Alfa Aesar) sheets were cut into 5 × 5 mm squares and used as metallic reference materials in this study. AZ31 was included in this study since it has been used previously as a reference material for the investigation of Mg-based materials [40–42]; likewise, NiTi was included due to the widespread use for cardiovascular stents [43].

Additionally, 90:10 polylactic-co-glycolic acid (PLGA) was included in this study as a non-metallic reference material due to the use of PLGA-based coatings to control the degradation of Mg-based materials for cardiovascular stents [43,44]. The PLGA samples were prepared by spin coating onto the non-tissue culture treated glass (Cat# 12-544-1; Fisher Scientific, Hampton, NH, USA), which was cut into 5 × 5 mmsquares followed by rough polishing with 240 grit SiC paper to improve the glass-PLGA adhesion. The 90:10 PLGA(Cat# AP49; Polyscitech, West Lafayette, IN, USA) was dissolved in chloroform at 10 wt/vol% and sonicated for 1 h at 40 °C. Subsequently, 50 μL of the dissolved PLGA was spin coated (SC100; Smart Coater Co., Saint Louis, MO, USA) onto the rough-polished glass substrates at 1300 RPM for 60 s. The PLGA coatings had a thickness of 64.0 ± 12.6 μm.

2.2. Microstructure characterization

The microstructure and surface elemental composition/distribution of the ZSr41 alloys, pure Mg control, and AZ31 reference were characterized using a scanning electron microscope (SEM; Nova NanoSEM 450, FEI Co., Hillsboro, OR, USA) equipped with an X-Max50 detector and AZtecEnergy software (Oxford Instruments, Abingdon, Oxfordshire, UK). The samples were ground with SiC abrasive paper (Ted Pella Inc., Redding, CA, USA) up to 1200 grit, and fine polished up to 0.25 μm with polycrystalline diamond paste (Physical Test Solutions, Culver City, CA, USA). Surface elemental composition and distribution were analyzed with energy dispersive X-ray spectroscopy (EDS). SEM images and EDS analyses were acquired with an accelerating voltage of 20 kV.

2.3. Electrochemical testing

Potentiodynamic polarization (PDP) curves were obtained using a three-electrode cell configuration connected to a potentiostat (Model 273A, Princeton Applied Research, Oak Ridge, TN, USA) and acquired with PowerSuite 2.50.0 software (Princeton Applied Research). Specific details pertaining to preparation of the working electrode are given elsewhere [29]. Briefly, the ZSr41 alloys, Mg control, and AZ31 reference samples (working electrode) were embedded in epoxy resin (0.5 cm^2 area exposed). Platinum foil and a silver/silver chloride (Ag/AgCl) were used as counter and reference electrodes, respectively. Prior to electrochemical experiments, the working electrode was ground with SiC abrasive paper up to 1200 grit and ultrasonically cleaned in acetone and ethanol. Revised simulated body fluid (r-SBF; pH 7.4, 37.5 °C) was used as the electrolyte for PDP scans (no equilibration, 0.5 to −3.5 V, 20 mV s^{-1}) since the ionic composition of r-SBF is the same as human blood plasma [45]. PDP curves were then extrapolated according to ASTM G102-89 standard to obtain values for corrosion potential (E_{corr}) and corrosion current density (J_{corr}). All potentials are in reference to Ag/AgCl electrode.

2.4. HUVEC responses and in vitro degradation of ZSr41 alloys

2.4.1. Preparation of HUVEC culture—Human umbilical vein endothelial cells (HUVECs; Cat# C2519A; Lonza Walkersville Inc., Walkersville, MD, USA) were cultured according to the manufacturer's recommended culture protocol to passage 5 in complete Endothelial Cell Growth Medium-2 (EGM™-2) media (Cat# CC-3162; Lonza Walkersville Inc.) in standard cell culture conditions (37 °C, 5%/95% CO_2/air, sterile, humidified

environment). Cell morphology was observed at each passage using an optical microscope to ensure HUVECs were normal and healthy.

2.4.2. Direct culture of HUVECs with ZSr41 alloys—Prior to cell culture experiments, all metallic samples were ground with SiC abrasive paper up to 1200 grit, ultrasonically cleaned for 15 min in separate baths of acetone and ethanol, and disinfected under ultraviolet (UV) radiation for 4 h on each side. The as-coated PLGA samples were disinfected by immersing in 70% ethanol for 20 min. Additionally, non-tissue culture treated glass slides (non-coated with PLGA) were cut into 5 × 5mm squares, cleaned in acetone and ethanol, disinfected under UV radiation, and used as a reference material for cell culture experiments. All the samples were placed in standard 12-well cell culture treated plates and rinsed with 3 mL of phosphate buffered saline (PBS) to calibrate the osmotic pressure. Subsequently, HUVECs (P5) were seeded directly onto the surfaces of the samples at a density of 6×10^3 cells cm^{-2} and incubated in 3 mL of EGM™-2 under standard cell culture conditions for 4 and 24 h. HUVECs cultured in EGM™-2 media supplemented with 10 ng/mL of tumor necrosis factor α (TNFα; Cat# PHC3015; Life Technologies, Carlsbad, CA, USA) was used as a positive control for VCAM-1 expression experiments; this group was designated as “HUVEC + TNFα”. A positive control for HUVEC adhesion and negative control for VCAM-1 expression, designated as “HUVEC” group, consisted of HUVECs cultured only with EGM™-2 in the wells, i.e. without any samples or TNFα stimulation. EGM™-2 alone was also used as a blank reference and designated as “EGM-2” group. Separate sets of samples were used for the 4 and 24 h adhesion experiments, and for the 4 and 24 h inflammation experiments.

2.4.3. Characterization of the HUVECs in direct contact with ZSr41 alloys—The interface between the HUVEC culture and ZSr41 alloys, and all other reference materials was characterized using SEM following the 4 and 24 h *in vitro* cultures. Additionally, corresponding surface elemental composition and Mg Kα1 elemental distribution maps were acquired with EDS. Specific details for sample preparation for *direct contact* analysis are published previously [29]. Briefly, the samples were removed from the wells, dip-rinsed in PBS fixed with 3% glutaraldehyde in 0.1 M potassium phosphate buffer, and again dip-rinsed in PBS. Subsequently, the samples were serially dehydrated in ethanol, critical-point dried (Autosamdri-815, Tousimis Research Corp., Rockville, MD, USA), and sputter coated (Model 108, Cressington Scientific Instruments Ltd., Watford, UK) with platinum/palladium.

2.4.4. Quantification of HUVEC adhesion under direct versus indirect contact conditions—HUVEC adhesion (i) under *direct* contact with the sample and (ii) under *indirect* contact with the sample, following the 24 h *in vitro* culture was evaluated using fluorescence microscopy. The results from the culture plates were grouped separately and designated as “plate”. Specific details for sample preparation for *direct/indirect contact* analysis through fluorescence microscopy are described previously [29]. Briefly, the samples in *direct* contact with HUVECs were dip-rinsed in PBS and the corresponding wells were washed separately with PBS. Subsequently, the samples and wells were separately fixed with 4% formaldehyde (VWR, Radnor, PA, USA), followed by incubation in Alexa Fluor

488® phalloidin (Cat# A12379; Life Technologies) and 4′,6-diamidino-2-phenylin dole dilactate (DAPI; Cat# D1306; Invitrogen™, Life Technologies) to fluorescently label cellular F-actin and nucleus, respectively. Adherent cells were visualized using a fluorescence microscope (Eclipse Ti and NIS software, Nikon, Melville, NY, USA) with a 10× objective lens at the same exposure condition and analyzed using Image J (NIH, Bethesda, MD, USA). Cell adhesion per group per time point was quantified by counting the DAPI-stained cell nuclei at: five and nine random locations on the sample surface and on the culture plate, respectively. Cell adhesion density was calculated as the number of adherent cells per unit area.

2.4.5. Quantification of HUVEC inflammatory response to the degradation of ZSr41 alloys in indirect contact—The inflammatory response of HUVECs to the degradation of ZSr41 alloys was evaluated using immunofluorescence of VCAM-1 and were carried out only for the cells in *indirect* contact with the samples (i.e. adhered to the tissue culture plates). The cells adhered to the culture plates were fixed with 4% formaldehyde for 20 min, incubated with 5% goat serum in PBS during 1 h for blocking, incubated with 10 μg/mL VCAM-1 (Cat# SC-13160; Santa Cruz Biotechnology Inc., Dallas, TX, USA) mouse anti-human primary IgG overnight at 4 °C, and incubated with 10 μg/mL goat anti-mouse secondary IgG-FITC (Cat# SC-2010; Santa Cruz Biotechnology Inc.) at room temperature for 1 h. The nuclei were subsequently stained with DAPI nucleic acid stain for 5 min. Five FITC images (640 × 512 pixel digital resolution, 16-bit depth, and 4 s exposure) per well per group were captured using a Nikon Eclipse T*i* fluorescence microscope. A mean fluorescence intensity signal per pixel was calculated using ImageJ and the method described by Patapova et al. [46].

2.4.6. In vitro degradation of ZSr41 alloys in the HUVEC culture—The *in vitro* degradation of the ZSr41 alloys, Mg, and AZ31 after the 4 and 24 h cultures was evaluated through measurements of pH and ionic concentrations of the collected media. The pH of the media was measured immediately after collection using a calibrated pH meter (Model SB70P, VWR). The concentration of Mg^{2+}, Zn^{2+}, and Sr^{2+} ions in the collected media ($[Mg^{2+}]$, $[Zn^{2+}]$, and $[Sr^{2+}]$, respectively) was measured using inductively coupled plasma optical emission spectrometry (ICP-OES; Optima 8000, Perkin Elmer, Waltham, MA, USA). In order to minimize the matrix effects in ICP-OES, the collected EGM™-2 aliquots were diluted to 1:100 solutions in DI water to measure $[Mg^{2+}]$ and $[Sr^{2+}]$. Ionic concentrations were then obtained from calibration curves generated using Mg and Sr standards (Perkin Elmer) diluted to ranges of 0.5–5.0 and 0.1–1.0 mg/L, respectively. The $[Zn^{2+}]$ in the EGM™-2 at 4 and 24 h were measured by diluting the collected aliquots to 1:7 solutions in DI water and then obtained using a calibration curve generated using a Zn standard (Perkin Elmer) diluted to a range of 10–1000 μg/L.

2.5. Effects of media alkalinity and Mg^{2+} ion concentration on HUVEC viability and morphology

To identify which factor(s) modulated HUVEC viability or morphology, separate experiments evaluating the effects of increasing $[Mg^{2+}]$ and increase in pH in the cell culture media were carried out. HUVECs (P5) were seeded in standard 12-well cell culture treated

plates at a density of 6×10^3 cells cm^{-2} and incubated in 3 mL of EGM™-2 under standard cell culture conditions for 24 h. The cell density after this initial 24 h stabilization period was designated as "EGM-2 (t = 0)." Subsequently, the media was removed and replenished with 3 mL of (i) EGM™-2 with pH values intentionally adjusted to 8.1, 8.5, 9.0, and 9.5, or (ii) EMG-2 supplemented with respective [Mg^{2+}] of 1.3, 2.6, 6.7, 13.1, 21.2, and 27.6 mM. EGM™-2 media without pH adjustment and without supplemented Mg^{2+} ions was used as a control in the pH and Mg^{2+} ion experiments, respectively. EGM™-2 incubated without cells was used as a blank reference. HUVECs were then incubated under standard cell culture conditions with the adjusted media conditions for another 24 h. Specific details used for adjusting pH and instructions for supplementing Mg ions using $MgCl_2 \cdot 6H_2O$ are described elsewhere [29,47]. After 24 h, adhered cells were fixed and stained, and viability was analyzed and quantified using the same method described above. Cell morphology was quantified by manually outlining twenty cells per image per group (on the cell culture plate) in ImageJ and obtaining values for average F-actin area per HUVEC nucleus, and Feret diameter aspect ratio of cells (D_{max}/D_{min}). D_{max} is the maximum Feret diameter. D_{min} is the minimum Feret diameter. The culture media was also collected and analyzed for changes in pH and [Mg^{2+}] as described above.

2.6. Statistical analyses

All experiments described above were done in triplicate. All data sets were tested for normal distribution and homogeneous variance. Parametric data sets were analyzed using one-way analysis of variance (ANOVA) followed by the Tukey HSD *post hoc* test. Data sets with normal distribution but heterogeneous variance were analyzed using one-way ANOVA (homogeneous variance not assumed) followed by the Games-Howell *post hoc* test. Nonparametric data sets were analyzed using the Kruskal-Wallis test followed by the Nemenyi *post hoc* test. Statistical significance was considered at $p < 0.05$.

3. Results

3.1. Microstructure of ZSr41 alloys

Fig. 1 shows the surface microstructures and elemental compositions of the ZSr41 alloys, pure Mg control, and AZ31 reference. SEM images at a low magnification of 600× (Fig. 1a) confirmed an increase in intermetallic β-phase with increasing Sr content in the ZSr41A-D alloys, respectively. As expected, the pure Mg control showed a surface free of secondary phases, and the AZ31 reference showed the presence of an intermetallic β-phase. SEM images at a high magnification of 5000× (Fig. 1a, insets) showed that the intermetallic β-phase of ZSr41A had a morphology of finely dispersed precipitates whereas coarse precipitates were observed on ZSr41B-D. Fig. 1b shows the quantification of surface elemental composition of the ZSr41 alloys, Mg, and AZ31 samples using EDS area analysis at a 600× magnification. Increasing Sr content was detected for each of the ZSr41 alloys; specifically (in wt%), 0.16 for A, 0.21 for B, 0.43 for C, and 1.18 for D. Additionally, a Zn content in close agreement to the nominal 4 wt% and 1 wt% was measured for the ZSr41A, B, D alloys and AZ31, respectively; the Zn content for ZSr41C was 2.6 wt%, which was slightly below the nominal value, possibly due to the metallurgical processing of the alloy. Furthermore, all samples had a predominant Mg content (>86.7 wt%), as well as Carbon (C)

content (~7.0 wt%), and Oxygen (O) content (~1 wt%). AZ31 was confirmed to contain 3.27% Aluminum (Al), 1% Zn, and traces of Manganese (Mn).

The composition of the α-matrices and β-phases (in at%) of the ZSr41 alloys was determined through EDS point analyses (Fig. 2) at the Points 1–8 shown in Fig. 1a. Comparison of the composition of the α-matrices of each ZSr41 alloy at the Points 1, 3, 5, 7 showed a similar elemental content irrespective of nominal Sr content in the alloy (Fig. 2a and b). Specifically, the α-matrices of all four ZSr41 alloys showed a Zn content of ~1.5 (i.e.~4 wt%), O content of ~1%, and C content of ~10%; these results are presented graphically in the histogram shown in Fig. 2b. In contrast, comparison of the composition of the intermetallic β-phases of each ZSr41 alloys at the Points 2, 4, 6, 8 (Fig. 2c) showed that the β-phases in the ZSr41B alloy (Point 4) and ZSr41D (Point 8) alloy had a higher Zn content than the ZSr41A (Point 2) and ZSr41C (Point 6). However, the Sr content was ~4 at % in the β-phases of all four ZSr41 alloys, irrespective of the alloy. Additionally, a higher O content of 11.7% was found in the β-phase of ZSr41A compared with the other three ZSr41 alloys (~1.3%). A trace amount of Calcium (Ca) was also detected in the β-phases of all ZSr41 alloys. The composition of the β-phases of the ZSr41 alloys is shown graphically in the stacked histogram in Fig. 2d. The Zn/Sr atomic ratio was calculated for the β-phases of the four ZSr41 alloys and is shown in Table 1. Comparison of the Zn/Sr atomic ratio showed that ZSr41B and ZSr41D had Zn/Sr ratios of ~1.6 and 1.7, respectively, while ZSr41A and ZSr41C had Zn/Sr ratios of 0.4 and 0.9, respectively.

3.2. Corrosion properties of ZSr41 alloys based on electrochemical testing

PDP curves of the polished samples showed that the initial degradation behavior of the ZSr41 alloys, pure Mg control, and AZ31 reference were similar (Fig. 3). The median PDP trace with the most representative E_{corr} and J_{corr} for each sample type was plotted in Fig. 3a. A qualitative assessment of the PDP curves indicated that the as-polished AZ31 reference showed the most cathodic behavior when compared to all the other Mg-based materials tested, all of which showed similar behavior. The samples would corrode faster if they were more anodic and corrode slower if they were more cathodic. Furthermore, assessment of the linear anodic (b_a) and cathodic (b_c) portions of the PDP curves gave indication that AZ31 and Mg had similar half-reaction characteristics in contrast to those for all ZSr41 alloys. PDP results do not typically yield absolute corrosion rates, but serve as an indication of the severity of the corrosion that is occurring at a select point in time in a particular electrolytic solution [48]; references [48,49] provide ample information on the use of PDP for studying the *in vitro* corrosion of Mg alloys. ANOVA was used to confirm statistically significant differences in the E_{corr} [$F(5, 12) = 18.114$, $p = 3.209 \times 10^{-5}$] and J_{corr} [$F(5, 12) = 6.7707$, $p = 3.22 \times 10^{-3}$] values calculated by Tafel extrapolation from the PDP curves (Fig. 3b). *Post hoc* pairwise comparisons confirmed that the E_{corr} of AZ31 (−1.42 ± 0.01 V) was significantly more cathodic ($p < 0.001$), when compared with ZSr41A (−1.52 ± 0.01 V), ZSr41B (−1.51 ± 0.01 V), ZSr41C (−1.55 ± 0.02 V), ZSr41D (−1.51 ± 0.02 V), and Mg (−1.57 ± 0.03 V). In contrast, Mg was significantly more anodic ($p < 0.01$) when compared with ZSr41A, ZSr41B, and ZSr41D. In addition, *post hoc* pairwise comparisons also confirmed a statistically significant higher J_{corr} ($p < 0.001$) for AZ31 (67.51 ± 5.47 mA cm

$^{-2}$) when compared with ZSr41A (39.99 ± 5.68 mA cm^{-2}) and ZSr41B (40.07 ± 6.47 mA cm^{-2}).

3.3. HUVECs in direct contact with ZSr41 alloys

A qualitative analysis of the HUVEC-substrate interface showed changes in surface topography and elemental composition for the ZSr41 alloys compared with the Mg control and reference materials as early as 4 h after incubation. Fig. 4a shows SEM micrographs of the cell-substrate interface for the materials investigated at an original magnification of 150× (Fig. 4a) and 1000× (Fig. 4a, insets) after 4 h of direct culture and *direct* contact with the samples. Adhered cells were observed on the surfaces of all samples; however, the cells attached on all the Mg-based materials (i.e. ZSr41 alloys, Mg, and AZ31) showed relatively compact cell bodies compared with the highly spread cells observed on the NiTi, PLGA, and glass samples. These two distinct cell morphologies were referred to as anisotropic and isotropic spreading, respectively [29,50]. Furthermore, comparison of cell attachment on the non-Mg-based samples showed that cells on both NiTi and glass were isotropically-spread almost completely flat on the surface of the samples whereas cells on the PLGA were isotropically-spread but not completely flat on the surface. Additionally, all Mg-based samples showed similar distribution of degradation-induced surface cracks, indicating similar degradation characteristics after 4 h of incubation in EGM™-2 media. Fig. 4b shows composite images of SEM micrographs with EDS elemental distribution maps (red = Mg, green = C, yellow = O, pink = Potassium (K) and Sodium (Na), orange = Phosphorus (P), purple = Ca, blue = Zn, white = Sr). The SEM-EDS composite images allowed visualization of the cell-biomaterial interface and confirmed cell adhesion directly on the surface of all Mg-based materials after 4 h of incubation. Interestingly, all Mg-based materials showed co-localization of Ca, P, and O which indicated that Mg degradation possibly attracted mineral deposition [29]. Fig. 5 shows elemental distribution maps of Mg (Kα1 lines) and a summary of elemental composition (in wt%) results obtained from EDS analyses at 150× magnification of the samples after the 4 h incubation. All Mg-based materials showed a similar surface distribution of Mg (Fig. 5a), giving further indication of similar degradation characteristics after 4 h of incubation. The stacked histogram shown in Fig. 5b summarizes the elemental composition (in wt%) results obtained from EDS analyses at 150× magnification. A Zn content comparable to the nominal 4% was detected on the surfaces of alloys ZSr41A, B, C, and D (4.47%, 4.28%, 3.01%, and 4.68%, respectively); Zn was also detected on AZ31 (0.96%) but not on the Mg control or any of the other reference materials. Additionally, increasing Sr content was also detected on alloys ZSr41B, C, and D (0.03, 0.31, and 0.66%, respectively); Sr was not detected on the surface of ZSr41A alloy, Mg control, or any of the reference materials. The deposition of Ca, P, and O was approximately equal and only observed on all Mg-based materials. In contrast, none of the reference materials (i.e. NiTi, PLGA, glass) showed deposition of Ca and P. Additionally, as expected, elemental composition in NiTi was predominantly Nickel (Ni) and Titanium (Ti), PLGA was predominantly C and O, and the glass sample had typical composition of soda-lime glass [29]. Lastly, all samples showed C content (attributed to adhered cells, proteins, and extracellular matrix produced by cells), and Na and K content (attributed to salt precipitation from soluble ions in the culture media).

Similarly, SEM and EDS analyses of the HUVEC-substrate interface after 24 h of incubation showed further changes in surface topography and elemental composition of the biomaterials investigated. Fig. 6 shows SEM micrographs of the cell-substrate interface at an original magnification of 150× and 1000× (Fig. 6, insets) after 24 h of direct culture and *direct* contact with the samples. In contrast to the 4 h samples, adhered cells were not observed on the surface of any of the ZSr41 alloys or Mg control. Some cell attachment was observed on the AZ31 sample but these HUVECs showed abnormal morphology. Additionally, isotropically-attached cells were observed on the surfaces of NiTi, PLGA, and glass reference materials. Similar to the 4 h time point, the cells attached on the surface of NiTi and glass continued to spread until almost completely flat while the cells on PLGA sample did not appear to spread completely flat. At the 24 h time point, the cell monolayer on the glass sample was approximately 80–90% confluent. Furthermore, comparison of the surface morphology and degradation-induced crack distribution showed that all of the ZSr41 alloy and AZ31 samples had similar characteristics after the 24 h incubation in EGM™-2 media. In contrast, the Mg control sample showed much larger cracks than the other Mg-based materials of this study. Fig. 7 shows elemental distribution maps of Mg (Kα1 lines) and a summary of elemental composition (in wt%) results obtained from EDS analyses at 150× magnification of the samples after the 24 h incubation. Surface distribution of Mg (Fig. 7a) showed heterogeneous distribution likely indicative of localized corrosion; the bright spots in each image corresponds to regions of higher Mg content (most evident in Fig. 7a, Mg). These images showed the varying degree of surface integrity of all of the Mg-based materials after 24 h of culture in EGM™-2 media, with AZ31 showing the most homogeneous surface. The stacked histogram shown in Fig. 7b summarizes the elemental composition (in wt%) results obtained from EDS analyses at 150× magnification. Similar to the 4 h time point, a Zn content comparable to the nominal 4% was detected on the surfaces of ZSr41 alloys and AZ31 but not on the Mg control or any of the other reference materials. Additionally, increasing Sr content was also detected on alloys ZSr41B, C, and D but not on ZSr41A alloy, Mg control, or any of the reference materials. All Mg-based samples continued to show similar content and co-localization of Ca, P, and O; however, the Ca content was slightly higher and the P content was slightly lower for all samples than their 4 h counterparts. The NiTi, PLGA, and glass samples showed very similar surface compositions compared to their 4 h counterparts and continued to show a lack of deposition of Ca and P. Lastly, all samples showed C, and Na and K content.

3.4. HUVEC adhesion under direct and indirect contact conditions

HUVEC adhesion directly onto the sample (*direct* contact) and on the culture plate (indirect contact) was evaluated at 4 and 24 h after direct culture with the ZSr41 alloys, Mg control, and reference materials, and results are summarized in Fig. 8. Fig. 8a shows fluorescence images of HUVECs attached to the culture plates at 24 h post-incubation; similar images were obtained for the 4 h culture on both direct and *indirect* contact, and for the 24 h *direct* contact. The DAPI-stained nuclei were used to quantify cell adhesion density at the 4 and 24 h time points and results are plotted in the histograms shown in Fig. 8b for HUVECs adhered to the culture plates and Fig. 8c for HUVECs adhered directly onto the samples. Results from cell adhesion density on the culture plate at 4 and 24 h (Fig. 8b) showed no statistically significant differences among all the groups evaluated. A comparison between

cell adhesion densities at 24 h with their respective counterparts at 4 h on the culture plates showed an increasing trend for almost all the samples, indicating possible early signs of proliferation. In all cases, the mean adhesion density at 24 h was within the range of error of the 4 h values. Results from cell adhesion density directly on the sample surface at 4 h (Fig. 8c) showed no statistically significant differences; in contrast, the Kruskal-Wallis test showed a statistically significant difference in the mean adhesion density at the 24 h time point [X^2 (8, N = 27) = 19.676, $p = 0.017$]. *Post hoc* pairwise comparisons showed a significantly lower adhesion density on both ZSr41A ($0.32 \pm 0.20 \times 10^3$ cells cm^{-2}) and ZSr41D ($0.30 \pm 0.22 \times 10^3$ cells cm^{-2}) compared with the glass reference ($3.81 \pm 0.89 \times 10^3$ cells cm^{-2}; $p < 0.05$). A comparison between cell adhesion densities at 24 h with their respective counterparts at 4 h on the sample surface showed a large decrease for all groups except for the glass reference indicating detrimental conditions for HUVEC adhesion and viability in the longer culture period.

3.5. HUVEC inflammatory response under indirect contact

Results from the inflammatory response, as indicated by the immunofluorescence expression of surface marker VCAM-1, are summarized in Fig. 9. The inflammatory response was only measured on HUVECs under *indirect* contact since adhesion density for *direct* contact was greatly reduced after 24 h of incubation. Fig. 9a shows immunofluorescence images of VCAM-1 expression (with DAPI-stained nuclei) of HUVECs attached to the culture plates at 4 h post-incubation; similar images were obtained for the 24 h time point. The mean VCAM-1 fluorescence intensity signal per pixel at the 4 and 24 h time points are plotted in the histograms shown in Fig. 9b and c, respectively. ANOVA (without homogeneous variance) was used to show statistically significant differences in the mean VCAM-1 expression at 4 h post incubation (Fig. 9b) [$F(10, 9) = 22.715$, $p = 5.191 \times 10^{-5}$]. *Post hoc* pairwise comparisons showed a significantly lower fluorescence intensity for the ZSr41A (159.9 ± 4.2 A.U.) and HUVEC (negative control; 136.2 ± 10.9 A. U.) groups than both the ZSr41D (267.4 ± 5.7 A. U.) and HUVEC + TNFα (positive control; 322.7 ± 11.3 A. U.) groups. Analysis of VCAM-1 intensity at the 24 h time point (Fig. 9c) showed no statistically significant differences. Interestingly, despite the lack of significant differences, a trend of increasing VCAM-1 fluorescence intensity was observed with increasing Sr content in the ZSr41 alloys.

3.6. In vitro degradation of ZSr41 alloys in the HUVEC culture

Results from the analysis of the culture media at the 4 h time point are summarized in the histograms shown in Fig. 10. Media pH and [Mg^{2+}] are both important indicators of the degradation of Mg-based materials [48]; in addition, [Zn^{2+}] and [Sr^{2+}] were also measured to ensure concentrations remained below reported cytotoxic levels. The Kruskal-Wallis test showed statistically significant differences in the mean pH of the culture media at 4 h (Fig. 10a) [X^2 (11, N = 36) = 31.444, $p = 9.36 \times 10^{-4}$]. Specifically, *post hoc* pairwise comparisons showed a significantly higherpHfor AZ31 (8.13 ± 0.03) when than NiTi (7.82 ± 0.03; $p < 0.05$), PLGA (7.83 ± 0.04; $p < 0.05$), and the EGM-2 blank reference (7.78 ± 0.01; $p < 0.01$). Similarly, a significantly more alkaline media was measured for ZSr41A (8.01 ± 0.08) when compared with the EGM-2 blank reference ($p < 0.05$). In general, as expected, all of the Mg-based samples caused an increase in alkalinity of the media.

Furthermore, ANOVA was used to confirm a statistically significant difference in the mean [Mg^{2+}] in the culture media (Fig. 10b) [$F(11, 24) = 12.535$, $p = 1.99 \times 10^{-7}$]. Specifically, *post hoc* pairwise comparisonsshowed that the [Mg^{2+}] in ZSr41A (9.69 ± 0.15 mM) and ZSr41B (9.69 ± 0.34 mM) were both significantly higher ($p < 0.05$) compared with PLGA (8.92 ± 0.12 mM) and glass (8.78 ± 0.26 mM); ZSr41B was also significantly higher ($p < 0.05$) compared with the HUVEC cells-only control (8.93 ± 0.05 mM). Similarly, the [Mg^{2+}] in the culture media of ZSr41C (10.02 ± 0.11 mM), ZSr41D (10.09 ± 0.37 mM), and AZ31 (10.20 ± 0.15 mM) were all significantly higher ($p < 0.01$, $p < 0.001$, and $p < 0.001$, respectively) when compared with NiTi (8.98 ± 0.12 mM), PLGA, glass, HUVEC + TNFα (8.99 ± 0.17 mM), HUVEC, and EGM-2 blank reference (9.16 ± 0.58 mM). *Post hoc* pairwise comparisons also showed a significantly higher [Mg^{2+}] in the culture media of the pure Mg control (9.80 ± 0.16 mM; $p < 0.05$) when compared with NiTi, PLGA, glass, HUVEC + TNFα, and HUVEC cells-only control. Fig. 10c and d show [Zn^{2+}] and [Sr^{2+}], respectively, in the cell culture media after 4 h. ANOVA confirmed statistically significant differences in the mean [Zn^{2+}] in the media [$F(11, 24) = 4.0052$, $p = 2.17 \times 10^{-3}$]. *Post hoc* pairwise comparisons showed that the [Zn^{2+}] of ZSr41D (1.59 ± 0.34 μM) was significantly higher when compared with the pure Mg control (0.49 ± 0.09 μM; $p < 0.01$), NiTi (0.57 ± 0.22 μM; $p < 0.05$), PLGA (0.78 ± 0.27 μM; $p < 0.05$), glass (0.56 ± 0.03 μM; $p < 0.01$), and EGM-2 blank reference (0.65 ± 0.12 μM; $p < 0.01$). No statistically significant differences were confirmed for [Sr^{2+}] and all values were in the low single-digit μM range.

Results from the analysis of the culture media at the 24 h time point are summarized in the histograms shown in Fig. 11. ANOVA was used to confirm statistically significant differences in the mean pH of the culture media at 24 h (Fig. 11a) [$F(11, 24) = 69.008$, $p = 2.06 \times 10^{-15}$]. *Post hoc* pairwise comparisons showed a significantly more alkaline media for all Mg-based materials than the reference materials and controls ($p < 0.001$); however, no statistically significant differences were confirmed when comparing Mg-based materials amongst each other. Specifically, the culture media of ZSr41A (8.12 ± 0.02), ZSr41B (8.16 ± 0.01), ZSr41C (8.07 ± 0.06), ZSr41D (8.15 ± 0.03), Mg (8.10 ± 0.06), and AZ31 (8.11 ± 0.01) were all significantly more alkaline compared with NiTi (7.79 ± 0.02), PLGA (7.81 ± 0.03), glass (7.85 ± 0.02), HUVEC + TNFα (7.85 ± 0.02), HUVEC (7.87 ± 0.02), and EGM-2 (7.79 ± 0.02). Furthermore, ANOVA showed statistically significant differences in the mean [Mg^{2+}] of the culture media at 24h (Fig. 11b) [$F(11, 24) = 55.126$, $p = 3.542 \times 10^{-15}$]. *Post hoc* pairwise comparisons indicated that the [Mg^{2+}] in the media incubated with all Mg-based materials was significantly higher ($p < 0.001$) when compared with NiTi (9.14 ± 0.29 mM), PLGA (9.48 ± 0.24 mM), glass (9.52 ± 0.24 mM), HUVEC + TNFα (9.37 ± 0.07 mM), HUVEC cells-only control (9.29 ± 0.04 mM), and EGM-2 blank reference (9.22 ± 0.19 mM). Specifically, the [Mg^{2+}] for the Mg-based materials were as follows: ZSr41A (16.19 ± 0.94 mM), ZSr41B (19.53 ± 0.90 mM), ZSr41C (13.92 ± 1.50 mM), ZSr41D (18.12 ± 1.61 mM), Mg (14.18 ± 1.07 mM), and AZ31 (13.63 ± 0.28 mM). The following significant differences in [Mg^{2+}] were also confirmed: ZSr41B and ZSr41D were both significantly higher ($p < 0.001$) than ZSr41C, Mg, and AZ31; and ZSr41A was significantly lower ($p < 0.01$) than ZSr41B, but significantly higher ($p < 0.05$) than AZ31. Fig. 11c and d show [Zn^{2+}] and [Sr^{2+}], respectively, in the cell culture media after 24 h. ANOVA confirmed statistically significant differences in the mean [Zn^{2+}] (Fig. 11c) [$F(11,$

24) = 55.126, $p = 2.697 \times 10^{-14}$]. *Post hoc* pairwise comparisons showed that the [Zn^{2+}] in the media incubated with ZSr41A (47.91 ± 2.84 μM), ZSr41B (32.87 ± 6.34 μM), and ZSr41D (40.65 ± 12.39 μM) were all significantly higher ($p < 0.001$) when compared with Mg (0.65 ± 0.31 μM), AZ31 (2.13 ± 0.32 μM), NiTi (1.09 ± 0.35 μM), PLGA (1.09 ± 0.20 μM), glass (1.06 ± 0.39 μM), HUVEC + TNFα (0.86 ± 0.40 μM), HUVEC cells-only control (0.52 ± 0.06 μM), and EGM-2 blank reference (0.68 ± 0.08 μM). The [Zn^{2+}] in the media incubated with ZSr41C (8.24 ± 2.58 μM) was significantly lower ($p < 0.001$) than ZSr41A, ZSr41B, and ZSr41D; likewise, ZSr41A was significantly higher ($p < 0.01$) than ZSr41B. ANOVA also confirmed statistically significant differences in the mean [Sr^{2+}] (Fig. 11d) [$F(11, 24) = 35.955$, $p = 3.29 \times 10^{-12}$]. Specifically, *post hoc* pairwise comparisons showed a significantly higher [Sr^{2+}] ($p < 0.001$) in the media of ZSr41B (16.42 ± 7.34 μM) and ZSr41D (38.22 ± 4.91 μM) when compared with Mg (4.01 ± 1.37 μM), AZ31 (3.22 ± 1.56 μM), NiTi (3.94 ± 0.74 μM), PLGA (4.21 ± 2.46 μM), glass (3.13 ± 2.16 μM), HUVEC + TNFα (2.67 ± 1.76 μM), HUVEC cells-only control (4.91 ± 0.64 μM), and EGM-2 blank reference (4.04 ± 0.59 μM). Likewise, ZSr41D was also significantly higher ($p < 0.001$) when compared with ZSr41A (6.16 ± 1.87 μM), ZSr41B, and ZSr41C (8.76 ± 1.48 μM), and ZSr41B was significantly higher ($p < 0.05$) than ZSr41A. Compared with their 4 h counterparts, the [Zn^{2+}] and [Sr^{2+}] measured at 24 h represented a ten-fold increase.

The degradation rates of each ZSr41 alloy, pure Mg control, and AZ31 reference (given as a mass loss rate per unit area per day) are summarized in Fig. 12. These values were calculated by multiplying the [Mg^{2+}] of each group at 24 h (ICP-OES results in Fig. 11b) by the incubation volume of media (3 mL) and then dividing by the initial exposed surface area of each sample to obtain a degradation rate based on initial geometry of the sample. ANOVA confirmed statistically significant differences in the normalized degradation rates during the 24 h incubation period [$F(5, 12) = 7.628$, $p = 1.954 \times 10^{-3}$]. *Post hoc* pairwise comparisons showed that the degradation rates of ZSr41B (1.63 ± 0.54 mg cm^{-2} day^{-1}) and ZSr41D (1.67 ± 0.52 mg cm^{-2} day^{-1}) were both significantly higher ($p < 0.05$) when compared with ZSr41C (0.70 ± 0.18 mg cm^{-2} day^{-1}), Mg (0.72 ± 0.05 mg cm^{-2} day^{-1}), and AZ31 (0.49 ± 0.05 mg cm^{-2} day^{-1}).

3.7. Effects of media alkalinity and Mg^{2+} ion concentration on HUVEC viability and morphology

Fig. 13 shows the results for HUVEC viability and morphology after 24 h of incubation with the culture media intentionally adjusted to pH values of 8.1, 8.5, 9.0, and 9.5 and non-adjusted media (EGM-2). The lower end of pH 8.1 was selected because the degradation of the Mg-based materials in this study caused an increase in pH up to approximately 8.1 (Figs. 10a and 11a) without reducing cell viability (Fig. 8b). In contrast, the higher end of pH 9.5 was selected based on previous results that showed significantly reduce cell viability at pH 9.5 [29]. Fluorescence images of HUVECs after 24 h of culture in non-adjusted media and alkaline media conditions (Fig. 13a) showed attached and viable, and isotropically-spread cells. Fig. 13b summarizes results of pH measurements of the collected media after 24 h of incubation with HUVECs (“blank” designates EGM-2 media incubated without HUVECs). It was observed that the pH of all the adjusted culture media decreased after culture, when

compared with their initially-adjusted value, which was likely due to the pH buffering effect of EGM-2 and possible acidic metabolites produced by viable HUVECs. Specifically, the media adjusted to 8.1, 8.5, 9.0, and 9.5 changed to 7.74 ± 0.01, 7.82 ± 0.05, 7.89 ± 0.02, and 8.01 ± 0.02, respectively. The blank reference (without HUVECs) and non-adjusted media (EGM-2) had pH values of 7.79 ± 0.03 and 7.78 ± 0.02, respectively. Results of HUVEC adhesion density in the pH-adjusted media after the 24 h culture are summarized in Fig. 13c. Statistically significant differences in the mean cell adhesion density were confirmed by ANOVA [$F(4, 10) = 5.723$, $p = 0.01163$]. *Post hoc* pairwise comparisons showed a significantly lower cell adhesion density ($p < 0.05$) for cells cultured in the media adjusted to pH 9.5 ($2.92 \pm 0.15 \times 10^3$ cells cm^{-2}) than the cells cultured in media adjusted to pH 8.1 ($6.34 \pm 0.62 \times 10^3$ -cells cm^{-2}), pH 8.5 ($6.86 \pm 0.58 \times 10^3$ cells cm^{-2}), and pH 9.0 ($7.04 \pm 0.90 \times 10^3$ cells cm^{-2}). The HUVEC adhesion density after the 24 h stabilization period and before the 24 h culture with the adjusted media (EGM-2 (t = 0)) was $3.86 \pm 0.09 \times 10^3$ cells cm^{-2}. The HUVEC adhesion density after the stabilization period and 24 h incubation in EGM-2 was $4.59 \pm 1.33 \times 10^3$ cells cm^{-2}. Interestingly, although no statistically significant differences were detected, a general trend of increasing cell adhesion density with increasing transient media alkalinity up to pH 9.0 was observed. Fig. 13d and e summarize the size and shape of adhered HUVECs as indicated by F-actin area per nucleus of adhered cell and aspect ratio of cell diameter, respectively. No statistically significant differences were detected for either measurement as a function of increasing initial pH of culture media. However, the F-actin area of adhered HUVECs cultured in the media adjusted to pH 9.5 had a lower mean, indicating a possible correlation between the reduced cell adhesion density and the reduced area of cell spreading.

Fig. 14 shows the results for HUVEC viability and morphology after 24 h of incubation with the culture media supplemented with $[Mg^{2+}]$ of 0 (EGM-2), 1.3, 2.6, 6.7, 13.1, 21.1, and 27.6 mM. Fluorescence images of HUVECs in all media conditions supplemented with $[Mg^{2+}]$ (Fig. 14a) showed attached and viable, and isotropically-spread cells. Fig. 14b summarizes the $[Mg^{2+}]$ of the culture media analyzed after 24 h of culture with HUVECs. An increasing trend of $[Mg^{2+}]$ in the supplemented culture media was confirmed after 24 h. Culture media without supplemental Mg^{2+} ions and incubated for 24 h without cells (blank reference) had a $[Mg^{2+}]$ of 10.56 ± 0.18 mM, which is in close agreement with literature values for MCDB 131 media [51]. The formulation for EGM™-2 is proprietary, however, per the vendor, it is based on the formulation of the classical MCDB 131 media. Results of HUVEC adhesion density in the media supplemented with increasing $[Mg^{2+}]$ after the 24 h culture are summarized in Fig. 14c. ANOVA was used to confirm statistically significant differences in the mean adhesion density [$F(6, 14) = 5.406$, $p = 4.427 \times 10^{-3}$]. *Post hoc* pairwise comparisons did not detect a significant reduction in adhesion density for any of the supplemented $[Mg^{2+}]$ conditions tested. However, a significantly higher cell adhesion density was observed in the media supplemented with 2.6 mM $[Mg^{2+}]$ ($11.45 \pm 0.78 \times 10^3$ cells cm^{-2}) when compared with the non-supplemented media (EGM-2; $5.03 \pm 1.35 \times 10^3$ cells cm^{-2}; $p < 0.001$), media supplemented with 1.3 mM $[Mg^{2+}]$ ($5.83 \pm 1.13 \times 10^3$ cells cm^{-2}; $p < 0.001$), and media supplemented with 27.6 mM $[Mg^{2+}]$ ($6.40 \pm 0.78 \times 10^3$ cells cm^{-2}; $p < 0.01$). The HUVEC adhesion density after the 24 h stabilization period and before the 24 h culture with the adjusted media (EGM-2 (t = 0)) was $4.91 \pm 1.15 \times 10^3$ cells cm^{-2}.

Fig. 14d and e summarize the cell spreading area (F-actin area per adhered nucleus) and shape (cell aspect ratio) of adhered HUVECs, respectively, as a function of increasing supplemented [Mg^{2+}]. No statistically significant differences were detected for either measurement; however, a wider distribution of cell spreading area was observed for HUVECs grown in the media supplemented with 2.6 mM [Mg^{2+}].

4. Discussion

The degradation of four heat-treated ZSr41 crystalline Mg alloys and their interaction with HUVECs was investigated using the direct culture method to model and study possible cellular modulatory effects at the HUVEC/ZSr41 alloy interface *in vitro*. We also examined HUVECs on the culture plate surrounding the ZSr41 alloy samples to understand modulatory effects of solubilized degradation products. Our results showed for the first time that the degradation products of Zn-containing Mg-alloys could induce an initial expression of VCAM-1 in cultured ECs, thus providing evidence of a transient inflammatory activation of ECs representative of the early-stages inflammation.

4.1. Microstructure and degradation of ZSr41 alloys

The incremental addition of Sr to the ZSr41 alloy resulted in distinctive β-phase composition and morphology. Our results are in agreement with previous studies for age-hardened Mg-Zn-Sr alloys that showed the segregation of Zn and Sr predominantly in the precipitated phases accompanied by an α-matrix with ~4 wt % Zn [26,52,53]. Brar et al. suggested that the intermetallic β-phases in the Mg-4Zn-0.5Sr alloy were ternary compounds in the form of $Mg_xZn_ySr_z$ [52]. In contrast, Li et al. showed the presence of two distinct β-phases, namely $Mg_{17}Sr_2$ and $MgZn_2$, through transmission electron microscopy (TEM) analysis for the Mg-1Zn-0.8Sr alloy [53]. Similarly, previous results from our group also confirmed the presence of $Mg_{17}Sr_2$ and $MgZn_2$ in the Mg-4Zn-1Sr (ZSr41C) alloy through EDS and X-ray diffraction (XRD) analysis. Li et al. also suggested that the formation of the $Mg_xZn_ySr_z$ was strongly related to the Zn content in the Mg-Zn-Sr alloys. Collectively, results from these independent studies suggested a transition in β-phase composition and morphology that might be correlated to the Zn/Sr at% from the nominal composition of the Mg-Zn-Sr alloys (e.g. 10.9 Zn/Sr at% ratio for Mg-4Zn-0.5Sr; 1.7 Zn/Sr at% ratio for Mg-1Zn-0.8Sr; 5.3 Zn/Sr at% ratio for Mg-4Zn-1Sr). Critical Zn/X at% ratios that control secondary phase composition have been described in detail for the Mg-Zn-Ca alloy system [29]. Although a detailed TEM analysis is required to accurately identify the composition of the β-phases in the ZSr41A-D alloys presented in this study, it is reasonable to speculate that the higher Zn/Sr at% ratio in the secondary phases of the ZSr41B and ZSr41D alloys could correspond to the $MgZn_2$ phase while the lower Zn/Sr at% for ZSr41A and ZSr41C could correspond to the $Mg_xZn_ySr_z$ and/or $Mg_{17}Sr_2$ phase. Detailed discussions on the evolution of the microstructure during solidification, grain size, and mechanical properties of the Mg-Zn-Sr alloy system can be found in Refs. [26,52,53], and a thermodynamic evaluation with phase diagrams are presented in Ref. [54].

An increasing β-phase volume fraction with increasing Sr content was observed for the ZSr41A-D alloys and is consistent with previous reports in literature [27]. In this systematic

study, the samples were polished up to 0.25 μm polycrystalline diamond paste to show the morphology of the secondary phases in detail. When Sr increased from 0.15 wt% to 0.5–1.5 wt%, β-phase morphology transitioned from finely dispersed oxygen-rich precipitates to coarse particulates, and its volume fraction increased. Previous studies investigating Mg-Zn-Sr alloys for biomedical applications pointed out that the mechanical enhancement induced by solid-solution strengthening resulting from the increasing volume fraction of the β-phases must be carefully balanced by the detrimental effects of secondary phases on corrosion resistance [52,53]. Specifically, although the volume fraction of secondary phase is generally reduced by a lower percentage of alloying elements, the Zn/Sr at% ratio could play a critical role in dictating mechanical and corrosion properties of the Mg-Zn-Sr alloys. For example, Brar et al. and Li et al. showed that both yield strength (YS) and ultimate tensile strength (UTS) of Mg-Zn-Sr alloys increased with decreasing Zn/Sr at% ratio; Brar et al. observed this trend for increasing Zn content [52] while Li et al. observed the trend for increasing Sr content [53]. Additionally, in this study, the Zn/Sr at% ratio also dictated composition and morphology of the distinctive β-phases, both of which are critical factors for micro-galvanic corrosion (i.e. corrosion resistance of the alloy). In fact, Brar et al. reported a decrease in corrosion resistance with increasing Zn/Sr at% ratio in Hank's solution for heat-treated Mg-xZn-0.5Sr alloys [52]; likewise, Cui et al. reported an improved corrosion resistance in SBF for heat treated Mg-4Zn-xSr alloys with decreasing Zn/Sr at% ratio [55]; and, Xia et al. recently reported that corrosion resistance improved in 0.1 M NaCl for heat-treated Mg-1Zn-xSr alloys with decreasing Zn/Sr at% ratio [56]. This critical ratio effect was also observed in the Mg-4Zn-xCa alloy system, where optimal mechanical (i.e. YS, UTS, elongation) and corrosion properties were achieved for Mg-Zn-Ca alloys when ~1.2 < Zn/Ca at% < ~5 [29]. Other ternary polycrystalline Mg-Zn-X alloys, including X = Al [40,57–59], Ca [29,60,61], Yttrium [62], Zirconium [63], Mn [64,65], Si [65], and Selenium and Copper (Cu) [66], exhibited solution strengthening and β-phase-mediated corrosion. To highlight the significance and novelty of this study in comparison with the state-of-the-art, a thorough review on the history and current development of as-cast crystalline Mg-Zn-Sr ternary alloys is summarized in Table 2 [26–28,52–56,67].

The significantly faster *in vitro* degradation rate of ZSr41B and ZSr41D in EGM™-2 media after 24 h of incubation could potentially be correlated with the higher Zn/Sr at% ratio in the β-phase of these alloys than that in the secondary phases of ZSr41A and ZSr41C, and the corresponding micro-galvanic corrosion formed with the α-matrix. Fig. 15 shows a summary of the average daily degradation rate (mass loss rate) per unit area of the ZSr41 alloys in this study as a function of Zn/Sr at%, O content, and morphology of each respective β-phase. Results from PDP measurements and Tafel extrapolation of this study (Fig. 3) showed that the initial corrosion response of the four as-polished ZSr41 alloys had similar characteristics, i.e. similar E_{corr} values and J_{corr} in the same order of magnitude for all ZSr41 alloys. The similarity in E_{corr} and J_{corr} values for the ZSr41 alloys was likely due to a rapid initial oxidation, without stabilization, of the predominant α-Mg matrix upon immersion in r-SBF [48]. Furthermore, collective results from the 4 h time point (SEM-based qualitative assessment of the surface integrity of the samples, Fig. 4; the surface distribution of Mg acquired through EDS, Fig. 5; pH measurements of the media, Fig. 10a; and [$Mg2^{+}$] in the media, Fig. 10b) supported the conclusion that all Mg-based materials had

a similar initial corrosion behavior when incubated in complete EGM™-2 media. Additionally, the pH and [Mg^{2+}] measurements indicated that the degradation of all the Mg-based materials investigated induced significant changes in the media as early as 4 h of incubation. Previous studies confirmed that the degradation of Mg-based materials in buffered media caused a sharp increase in the pH after only hours of static incubation [68,69]. Analysis of the 24 h results showed differences in surface crack density and Mg surface distribution (Figs. 6 and 7), which could be the early signs of different long-term degradation behaviors. Moreover, the differences in the degradation profiles at 24 h were observed through the linearly-correlated pH and [Mg^{2+}] measured in the media (Fig. 11a and b). Specifically, the significant increase in both indicators induced by the degradation of ZSr41B and ZSr41D alloys, along with the normalized results shown in Fig. 12, are direct evidence of the faster degradation of these alloys. These results were in close agreement with a previous 72-h evaluation of the *in vitro* degradation of ZSr41 alloys with human embryonic stem cells (hESC) in mTeSR®1 media showing both higher pH and [Mg^{2+}] for ZSr41B and ZSr41D alloys than ZSr41A and ZSr41C [27]. Additionally, the 24-h degradation rates per unit surface area of the ZSr41 alloys in EGM™-2 media were in close agreement with the degradation rate per unit surface area measured during the first 24 h interval in mTeSR®1 media despite the differences in media composition (osmolality 260–290 mOsm/kg H_2O for EGM™-2 and 330–350 mOsm/kg H_2O for mTeSR®1). Table 3 summarizes the ionic concentrations from the inorganic salts, ionic strength, and osmolality of MCDB 131 (non-commercial analog of EGM™-2) [51], mTeSR®1 [47], r-SBF [45], and human blood plasma [47]. Osmolality values for EGM™-2 and mTeSR®1 were obtained from technical specification sheets from the vendors, while values for human blood plasma were obtained from [70].

The solubilized [Mg^{2+}], [Zn^{2+}], and [Sr^{2+}] in the media as a result from the degradation of the ZSr41 alloys during the 24 h incubation were below the therapeutic daily dosages (TDD) and LD50 reported in literature. The TDD and LD50 for Mg^{2+}, Zn^{2+}, and Sr^{2+} are summarized in Ref. [27]. The largest change in [Mg^{2+}] in the culture media induced by the degradation of the ZSr41 alloys in this study was observed for ZSr41B at 24 h (10.31 mM above the blank reference), which was well below the TDD of 24–40 mM and LD50 of 50–73 mM (multiple mammalian cell types). Specifically for ECs, Zhao et al. indicated that the LD50 of Mg^{2+} was 30 mM [71]. Likewise, the largest change in [Zn^{2+}] and [Sr^{2+}] in this study were both measured at 24 h for ZSr41A (47.22 μM [Zn^{2+}] above the blank reference) and ZSr41D (34.44 μM [Sr^{2+}] above the blank reference). Thus, the [Zn^{2+}] and [Sr^{2+}] concentrations measured in this study at 24 h were lower when compared with the TDD of 900 μM and LD50 of 3.7 mM for [Zn^{2+}], and TDD of 5.9 mM and LD50 of 33.8 mM for [Sr^{2+}].

4.2. HUVECs in indirect contact with ZSr41 alloys: viability and early inflammatory response

HUVEC adhesion density on the culture plate (*indirect* contact) up to 24 h was unaffected by the solubilized degradation products of the ZSr41 alloys, indicating adequate cytocompatibility. The absence of significant differences in the adhesion densities on the culture plates surrounding the ZSr41 samples compared with each other at 4 h and then at 24

h (Fig. 8b) indicated that HUVEC viability was unaffected by the varying degradation rates (and concomitant solubilized degradation products) of the Mg-based materials of this study. Specifically, at 24 h, HUVEC adhesion density was unaffected by the significantly higher degradation rates of ZSr41B and ZSr41D. Furthermore, our results confirmed unaltered HUVEC viability and morphology when cultured in the media "transiently-adjusted" to pH 9.0 (Fig. 13) or supplemented with $[Mg^{2+}]$ = 27.6 mM (Fig. 14). It is important to highlight that the media was "transiently-adjusted" to pH 8.1–9.5 in our alkalinity experiments, because the $NaHCO_3$/5% CO_2 buffer system in EGM™-2 media (and other mammalian cell culture media) could effectively buffer sharp increases in pH within minutes [72]. In the direct culture, however, the degradation of Mg induced pH change was continuous, which explained why the pH of the EMG™-2 media after 24 h of incubation with Mg-based materials (pH 8.07–8.16) was higher than that of the media "transiently-ad justed" to pH 9.5 (8.01) after 24 h of culture. Collectively, these results indicated that continuous but slight alkaline media would not affect HUVEC viability or morphology as much as sharp transient alkaline changes (i.e. pH 9.5). In contrast, $[Mg^{2+}]$ in the media from the degradation of the Mg-based materials (4.41–10.31 mM) and from the supplemented media experiment (27.6 mM) above the baseline (~10 mM) showed no detrimental effects on HUVEC viability or morphology, mainly because active transport of Mg^{2+} ions across the cell membrane is tightly regulated [73]. Interestingly, in our experiments, supplementing the EGM™-2 media with a $[Mg^{2+}]$ = 2.6 mM led to a significant increase in cell adhesion density. Zhao et al. also showed beneficial EC responses *in vitro* with a total of 13 mM $[Mg^{2+}]$ in the culture media (3 mM basal + 10 mM supplemented). Specifically, they reported enhanced proliferation rate of human coronary aorta EC (HCAEC) at 13 mM $[Mg^{2+}]$ followed by a gradual decrease up to 33 mM tested [71]. Conversely, previous *in vitro* studies showed that deficiency of Mg^{2+} ions (lower than 10 mM of the basal EGM™-2 media) inhibited HUVEC proliferation and migration [74,75]; collectively, these *in vitro* results indicated the biphasic effects of $[Mg^{2+}]$ in the culture media. Clinically, deficiency of Mg^{2+} ion was associated with cardiovascular conditions, including atherosclerosis, hypertension and thrombosis [74,75]. It has been shown that the *in vitro* effects of Mg^{2+} ions on cell behavior are dependent on cell type [29]; thus, the degradation rate should be carefully engineered to maximize the benefits for each end-goal application. The results of this study suggested that media alkalinity induced more dramatic effects on cellular functions than $[Mg^{2+}]$ from the degradation of Mg-based materials, which were in agreement with previous studies for bone marrow derived mesenchymal stromal cells (BMSCs) [29,76], UMR-106 rat osteosarcoma [77], and hESCs [47]. Overall, the cytocompatibility results of Mg-Zn-Sr alloys with HUVECs reported in this study were in general agreement with previous *in vitro* studies with hESCs [27] and fibroblasts [28,53,67].

Transient type II EC inflammatory activation, characterized by significantly enhanced VCAM-1 expression, could be induced by solubilized heavy metal ions in the culture media. We investigated the *in vitro* induction of VCAM-1 expression in HUVECs at 4 and 24 h based on the published literature showing that *in vitro* CAM induction by TNFα in ECs peaked at 4–6 h after stimulation and declined to basal levels by 24 h (refractory period) [78–80]. Additionally, when cells were allowed to reach confluency prior to stimulation (not used in this study), VCAM-1 induction by TNFα was expressed within hours of stimulation

and remained at high levels for at least 72 h [81]. Previous studies showed that the transient expression of CAMs including E-selectin, intercellular adhesion molecule-1 (ICAM-1), and VCAM-1 in cultured ECs could be induced by the exposure to non-cytotoxic concentrations of heavy metal ions. *In vitro* experiments with Ni^{2+} and Co^{2+} ion concentrations (in the form of $NiCl_2$, $NiSO_4$, $CoCl_2$, or $CoSO_4$) ranging from 0.1–2 mM were reported to induce the expression of all three CAMs at the mRNA and protein levels in a dose-dependent and transient manner; CAM induction by heavy metal ions was comparable to the induction by pro-inflammatory mediators such as TNFα, interleukin 1 (IL-1), and bacterial lipopolysaccharide (LPS) [7,15–21]. Additionally, Klein et al. observed CAM induction by Ni^{2+} and Co^{2+} ion concentrations in the mM and nM but not μM range, suggesting a possible biphasic CAM induction response to heavy metal ions [17]. Interestingly, other Period 4 transition metal ions such as Cr^{3+} (up to 1 mM) [7,19], Fe^{3+} [18], Mn^{2+}, and Cu^{2+} (both up to 2 mM) [16,18] did not induce CAM expression in cultured ECs. Previous studies showed that Ni^{2+} or Co^{2+} ions activated the auto-regulatory mechanism of the nuclear factor-κB/inhibitor of κB (NF-κB/IκB) system [16,18–20], up-regulated transcription factor activator protein-1 (AP-1) [19,20], but did not initiate a pro-inflammatory cytokine-induced autocrine stimulation [16,18]. The ubiquitous transcription factor NF-κB, and AP-1, are key regulators of cytokine-induced pro-inflammatory proteins, such as endothelial CAMs, cytokines, and growth factors among others [12,19]. Further mechanistic studies identified the involvement of phosphorylation events of different protein kinases of two or more signaling pathways leading to the translocation of NF-κB and subsequent CAM expression [18,20]. It was suggested that Ni^{2+} and Co^{2+}-induced CAM expression could be a result from metal ion attachment to proteins presented to the cultured ECs [20], due to the involvement of oxygen radicals [18,82], or due to the inhibition of the biological activity of nitric oxide [82]. More recent studies focused on the culture of ECs with bulk permanent implant materials and reported: no significant CAM expression after culture with NiTi, CoCrNi, or NiCr [21]; significant ICAM-1 and VCAM-1 expression induced by the ion release from Ti-6Al-4V alloy [22]; and significant E-selectin expression induced by the ion release from NiTi wires [23].

Early-stage inflammatory activation in HUVECs was not likely induced by the solubilized Mg^{2+} ions. Our results showed that a [Mg^{2+}] of 0.9 mM above baseline (pure Mg control; Fig. 10b) did not induce a significant VCAM-1 expression on the cultured HUVECs at 4 h (Fig. 9b). Although a [Mg^{2+}] of ~1.2 mM was measured for ZSr41D and AZ31, these alloys contained other alloying elements and the effects of Mg^{2+} ions could not be decoupled. Since the [Mg^{2+}] released into the culture media was in a similar range compared to Ni^{2+} and Co^{2+} (μM to mM range), and since no significant VCAM-1 expression was observed at either 4 or 24 h, it is reasonable to conclude that Mg^{2+} ions in the μM to low mM range (above the baseline of ~10 mM) do not transiently induce the expression of VCAM-1 on cultured HUVECs. However, previous *in vitro* studies showed that Mg^{2+} ion deficiency (i.e. below 10 mM) could induce the expression of VCAM-1 in cultured HUVECs [74,75]. Previous studies also showed that a supplemented [Mg^{2+}] higher than 40 mM caused discontinuities within the intercellular cell-to-cell junctions in cultured ECs [71], indicating possible mediation of EC inflammation. In fact, other studies showed that Mg^{2+} ions could

attenuate the NF-κB signaling pathway [83,84], thereby participating in multiple NF-κB-related cellular responses.

Zn^{2+}, another Period 4 transition metal ion, released at 4 h (Fig. 10c) could have been involved in the induction of VCAM-1 on HUVECs *in vitro* (Fig. 9b). The solubilized Zn^{2+} ions from the fast-degrading ZSr41D alloy possibly induced the early-stage inflammatory activation in HUVECs, providing the first *in vitro* evidence for an initial inflammatory response to the degradation of Zn-containing Mg-based biomaterials. The increase of VCAM-1 expression at 4 h of culture, however, could be a transient effect as early responses of ECs *in vitro*, considering that the cells recovered and showed no significant differences in VCAM-1 expression at 24 h of culture. Previous studies showed that Zn^{2+} ions (in the form of $ZnCl_2$) induced the following responses in cultured ECs: at [Zn^{2+}] of 1–10 nM, significantly increased the expression of both E-selectin and ICAM-1 after a 5 h incubation [17]; at [Zn^{2+}] of 1 μM and 1 mM, weakly induced the expression of NF-κB p65 mRNA after an 8 h incubation [19]; and at [Zn^{2+}] of 1 mM, increased the expression of E-selectin after a 5 h incubation [17] and ICAM-1 after a 4 h incubation [20]. Similar to Ni^{2+} and Co^{2+} ions, one mechanistic study provided evidence for the involvement of phosphorylation events of different protein kinases involved in the translocation of NF-κB and concomitant ICAM-1 induction by Zn^{2+} ions [20]. In fact, previous studies demonstrated the active role of Zn in the phosphorylation of IκB leading to the translocation of NF-κB in HUT-78 cells [85,86]. However, other CAM-related studies also reported the inability of Zn^{2+} ions to induce the expression E-selectin, ICAM-1, or VCAM-1 after a 6 h incubation with a [Zn^{2+}] of 2mM [16] and no E-selectin induction by a [Zn^{2+}] of 1 mM after a 4 h incubation [20] or 5 h incubation [19]. These seemingly contradictory results for [Zn^{2+}] in the mM range could be due to the close proximity to the TDD and LD50 for Zn^{2+} ions. In fact, Wagner et al. observed that HUVEC morphology at [Zn^{2+}] of 1 mM was strongly damaged [20]. Additionally, time-dependent CAM induction [16] in response to Zn^{2+} ions could lead to some of the discrepancies in published literature and should be systematically evaluated to identify distinct effects on the expression of E-selectin, ICAM-1, and VCAM-1 in cultured ECs. Although Zn^{2+} does not directly induce the formation of reactive oxygen intermediates via Fenton reaction (in contrast with Ni^{2+} and Co^{2+} [87]), varying [Zn^{2+}] has been shown to have an active role in the production of nitric oxide (NO) [88,89] and on the activity of Zn/Cu-superoxide dismutase (SOD) [90]; both NO and Zn/Cu-SOD have also been shown to have an effect on CAM expression in cultured ECs [91,92]. While Zn^{2+} ions resulting from the fast degradation of bulk Mg alloys might be responsible for initial VCAM-1 induction in cultured ECs *in vitro*, extensive literature of *in vivo* studies showed that Zn deficiency is associated with increased inflammatory responses [93,94]. Zn is considered as an antioxidant and *anti*-inflammatory agent in human and plays an important role in cell mediated immunity [95]. Zn supplementation in the elderly has shown decreased generation of inflammatory cytokines and decreased oxidative stress [95]. Additionally, Zn-containing Mg alloys with controlled degradation rates showed minimal inflammatory responses when implanted *in vivo* [33,34,36,96–98]. Further experiments with Zn^{2+} supplemented media are needed to determine the mechanisms responsible for the transient increase of VCAM-1 expression *in vitro*.

To our knowledge, a systematic evaluation of CAM induction by Sr^{2+} ions has not been reported in literature; thus, direct effects of Sr^{2+} ions are unknown. The absence of statistically significant differences in the [Sr^{2+}] of the culture media at 4 h presented in this study (Fig. 10d) indicated that the [Sr^{2+}] in the media of all groups was comparable. Specifically, the [Sr^{2+}] in the media of the negative control group for VCAM-1 expression (HUVEC group; 1.50 ± 1.31 μM) did not show an induction of VCAM-1 expression. Therefore, it is unlikely that Sr^{2+} ions in the low μM range would induce EC activation through VCAM-1 expression.

Our results from VCAM-1 expression at 4 h indicated a significantly higher response to ZSr41D most likely due to the significantly faster degradation of ZSr41D (compared with ZSr41A and ZSr41C) and concomitantly higher [Zn^{2+}] in the media. It is unlikely that VCAM-1 induction was caused by solubilized organic debris from dead cells because the similar values of adhered cells for all Mg-based materials under both direct and indirect contact suggest that the percentage of adhered live cells versus dead cells was similar for these samples.

In terms of clinical translation, an engineered activation of ECs (and concomitantCAMexpression) could help control the activation of macrophages during the distinct phases of the inflammatory response, leading to dampened inflammation throughout the foreign body response and resolution stages (biological response) or the degradation of the Mg-based materials (biomaterial response) [8,11]. Heavy metal ions including Zn^{2+}, Ni^{2+}, Co^{2+}, and Cr^{3+} were also shown to increase the activity of immune cells, e.g. polymorphonuclear neutrophil granulocytes (PMNs) [99], macrophages [100], and lymphocytes [101]. Interestingly, low concentrations of Zn^{2+} ions activated the secretion of pro-inflammatory mediators from PMNs and increased PMN-EC binding [99]. In contrast, Mg^{2+} ions did not induce detrimental immunomodulatory effects on cultured macrophages or dendritic cells [38,39], but modulated EC/macrophage adhesion via CAM expression [74,75].

Collectively, our results from the *in vitro* evaluation of VCAM-1 induction highlighted the critical importance of carefully engineering the degradation rates of Zn-containing Mg alloys to minimize the risks associated with early inflammatory responses when used for biomedical implant applications, such as cardiovascular stents, orthopedic implants, craniomaxillofacial devices, etc. Future studies are needed to determine the possible dose-dependent effect of Zn^{2+} and/or the effect of Zn^{2+} chelators on VCAM-1 induction in HUVECs to develop a comprehensive understanding of the ion-dependent mechanism. Further exploration of the effects of Zn-containing Mg-alloys and their roles in the activation of cells involved in inflammation will support the research effort toward superior alloy design for medical implant applications.

4.3. HUVECs in direct contact with ZSr41 alloys: cell-biomaterial interface

The dynamic interface between the degrading ZSr41 alloys and HUVECs cultured directly onto the sample surface showed signs of reduced cell adhesion *in vitro* after 24 h. The observed decrease in cell adhesion density for all Mg-based materials (24 h compared with 4 h; Fig. 8c) provided evidence of reduced EC growth directly on the sample surface. Our

results from the effects of [Mg^{2+}] on HUVEC viability and morphology supported the conclusion that the solubilized Mg^{2+} ions were unlikely involved in the reduction of cell adhesion observed. However, it is difficult to determine whether the reduction of cell adhesion between the 4 and 24 h intervals was due to a local increase in alkalinity, the changing surface topography, and/or the surface composition at the cell-biomaterial interface.

While a sharp increase in local alkalinity at the interface would be sufficient to reduce cell adhesion (Fig. 13c), the drastic change in surface topography between 4 h and 24 h could have also participated in reducing cell adhesion. Comparison between the corrosion-induced cracks and elemental Mg distribution at 4 h (Figs. 4a and 5a) and 24 h (Figs. 6 and 7a) showed a drastic change in the surface topography. It is also important to mention that the Zn/Sr ratio could affect the grain size and secondary phase morphology of Mg-Zn-Sr alloys, as well as composition. All these variances at the cell-material interface could work collectively in affecting cell attachment. The surface microstructure has been reported to play an important role in cell adhesion even when the other variances (e.g., composition) were fixed [102]. Previous *in vitro* studies using HUVECs and polymer-based substrates reported the ability of surface topography in the nm [103] and μm [104] ranges to accelerate cell adhesion, and to modulate proliferation [105]. Additionally, the surface elemental composition of this *in vitro* study closely resembled the post-implantation surface reported previously for an *in vivo* study in a murine artery [106]. Further experiments are needed in order to elucidate the respective effects of each factor on cells.

In a previous study, in which we investigated the dynamic interface between Mg-Zn-Ca alloys and BMSCs, we suggested that the changing surface topography of Mg-based materials could be heavily involved in mediating cellular responses [29]. In the Mg-Zn-Ca/BMSC study, BMSCs proliferated on the sample surface up to 72 h. In contrast, HUVEC viability reduced on the surface of the Mg-Zn-Sr alloys after only 24 h. Taken together, these observations could be indicative of: the sensitivity of HUVECs compared with BMSCs; the effect of alloying elements on cellular responses when cultured directly onto the sample surface; and/or, the distinct alloy degradation profile in distinct cell culture media. Cardiovascular biomaterials, including Mg-based materials, for stent applications are idealized to be hemocompatible (i.e. thromboresistant and reducing platelet adhesion), promote endothelialization, reduce neointimal hyperplasia, and have no pro-inflammatory properties [4,107]. The truncated HUVEC viability and increased platelet adhesion [28] at the cell-ZSr41 alloy interface indicated that the ZSr41 alloys (especially ZSr41D) need to be studied further to determine their applicability for cardiovascular stent applications. Previous *in vivo* and pre-clinical studies of cardiovascular stents showed the potential of Mg-based materials [4]; however, evidence of undesired neointimal hyperplasia and a desire to further reduce the degradation rate was reported in most cases. The *direct* culture method used in this study could thus be a valuable tool in studying the *in vitro* endothelialization, smooth muscle cell responses leading to neointimal hyperplasia, and immunomodulation, in order to engineer solutions to overcome current shortcomings of Mg-based materials for cardiovascular stenting or neurovascular embolization applications.

5. Conclusions

This article reported the cytocompatibility and early-stage inflammatory induction of human umbilical vein endothelial cells in response to the degradation of four Mg-4Zn-xSr alloys (x = 0.15, 0.5, 1.0, 1.5 wt%; designated as ZSr41A, B, C, and D respectively) in the direct culture *in vitro*. Possible factors and mechanisms that affect cellular responses were also investigated. The following major conclusions were drawn from the present study:

1. Addition of 0.5 or 1.5 wt% Sr to the heat-treated Mg-4Zn-xSr alloys resulted in a Zn-enriched coarse β-phase (Zn/Sr at% ~1.5). In contrast, addition of 0.15 or 1.0 wt% Sr resulted in a β-phase with a Zn/Sr at% < 1; however, the β-phase morphology in the Mg-4Zn-0.15Sr alloy consisted of finely dispersed precipitates while the Mg-4Zn-1.0Sr alloy had coarse precipitates. Furthermore, an increasing β-phase volume fraction with increasing Sr content was observed. Given that the *in vitro* degradation rates of the Mg-4Zn-0.5Sr and Mg-4Zn-1.5Sr alloys were greater than the other two Mg-4Zn-xSr alloys in this study, it was suggested that the Zn/Sr at% ratio could play a critical role in dictating corrosion, and perhaps mechanical properties of the Mg-Zn-Sr alloys.

2. HUVEC adhesion density on the culture plate (*indirect* contact) up to 24 h was unaffected by the solubilized degradation products of the Mg-4Zn-xSr alloys, indicating adequate cytocompatibility. The results also indicated that HUVEC viability is not negatively impacted when cultured in the media with pH up to 9.0 or in the media with supplemented [Mg^{2+}] up to 27.6 mM (maximum tested for [Mg^{2+}]).

3. Solubilized Zn^{2+} ions (in a non-cytotoxic range) resulting from the significantly faster degradation of Mg-4Zn-1.5Sr alloy possibly induced a transient higher VCAM-1 expression on HUVECs at the early-stage (4 h) of direct culture but *indirect* contact with the samples. The effects of the alloy samples on VCAM-1 induction were comparable to the effects of pro-inflammatory cytokine TNFα, thereby providing the first evidence for the transient early-stage inflammatory response to the degradation of Zn-containing Mg-based biomaterials.

4. The dynamic interface between the degrading Mg-4Zn-xSr alloys and HUVECs cultured *directly* onto the sample surface showed reduced cell adhesion *in vitro* after 24 h. However, based on the results of this study, it is difficult to determine whether the reduction of cell adhesion was due to a local increase in alkalinity, the changing surface topography, and/or the surface composition at the cell-biomaterial interface.

5. The *direct* culture method used in this study is proposed as a valuable tool in studying the design aspects of Mg-based cardiovascular biomaterials *in vitro*, such as: endothelialization, smooth muscle cell responses leading to neointimal hyperplasia, and immunomodulation, in order to engineer solutions to address current shortcomings of Mg-based materials for cardiovascular or neurovascular applications.

Acknowledgments

The authors would like to thank the American Heart Association (12SDG12220014), Hellman Faculty Fellowship (Huinan Liu), and the University of California Regents Faculty Fellowship (Huinan Liu) for financial support. Aaron F. Cipriano would like to thank the Graduate Division at UC Riverside for the Dissertation Year Program fellowship. The authors thank the Central Facility for Advanced Microscopy and Microanalysis (CFAMM) at the University of California, Riverside.

References

1. Staiger MP, Pietak AM, Huadmai J, Dias G. Magnesium and its alloys as orthopedic biomaterials: a review. Biomaterials. 2006; 27(9):1728–1734. [PubMed: 16246414]
2. Witte F, Hort N, Vogt C, Cohen S, Kainer KU, Willumeit R, Feyerabend F. Degradable biomaterials based on magnesium corrosion. Curr Opin Solid State Mater Sci. 2008; 12(5–6):63–72.
3. Zheng YF, Gu XN, Witte F. Biodegradable metals. Mater Sci Eng. 2014; 77:1–34.
4. Hermawan H, Dubé D, Mantovani D. Developments in metallic biodegradable stents. Acta Biomater. 2010; 6(5):1693–1697. [PubMed: 19815097]
5. Amini AR, Wallace JS, Nukavarapu SP. Short-term and long-term effects of orthopedic biodegradable implants. J Long Term Eff Med Implants. 2011; 21(2):93–122. [PubMed: 22043969]
6. Jiang Y, Jia T, Wooley PH, Yang S-Y. Current research in the pathogenesis of aseptic implant loosening associated with particulate wear debris. Acta Orthop Belg. 2013; 79(1):1–9. [PubMed: 23547507]
7. Kirkpatrick CJ, Krump-Konvalinkova V, Unger RE, Bittinger F, Otto M, Peters K. Tissue response and biomaterial integration: the efficacy of in vitro methods. Biomol Eng. 2002; 19(2–6):211–217. [PubMed: 12202185]
8. Franz S, Rammelt S, Scharnweber D, Simon JC. Immune responses to implants – a review of the implications for the design of immunomodulatory biomaterials. Biomaterials. 2011; 32(28):6692–6709. [PubMed: 21715002]
9. Belt HVD, Neut D, Schenk W, Horn JRV, Mei HCVD, Busscher HJ. Infection of orthopedic implants and the use of antibiotic-loaded bone cements: a review. Acta Orthop. 2001; 72(6):557–571.
10. Anderson JM. Chapter 4 Mechanisms of inflammation and infection with implanted devices. Cardiovasc Pathol. 1993; 2(Suppl 3):33–41.
11. Anderson JM, Rodriguez A, Chang DT. Foreign body reaction to biomaterials. Semin Immunol. 2008; 20(2):86–100. [PubMed: 18162407]
12. Pober JS, Sessa WC. Evolving functions of endothelial cells in inflammation. Nat Rev Immunol. 2007; 7(10):803–815. [PubMed: 17893694]
13. Cook-Mills JM, Marchese ME, Abdala-Valencia H. Vascular cell adhesion molecule-1 expression and signaling during disease: regulation by reactive oxygen species and antioxidants. Antioxid Redox Signal. 2010; 15(6):1607– 1638.
14. Sobieszczanska, B., Wawrzynska, M., BiaLy, D. Chapter 12 Immunological response of electrostatic charge at the surface of biomaterials. In: Tofail, S., editor. Biological Interactions with Surface Charge in Biomaterials. The Royal Society of Chemistry; London: 2012. p. 161-171.
15. Wildner O, Lipkow T, Knop J. Increased expression of ICAM-1, E-selectin, and VCAM-1 by cultured human endothelial cells upon exposure to haptens. Exp Dermatol. 1992; 1(4):191–198. [PubMed: 1285410]
16. Goebeler M, Meinardus-Hager G, Roth J, Goerdt S, Sorg C. Nickel chloride and cobalt chloride, two common contact sensitizers, directly induce expression of intercellular adhesion molecule-1 (ICAM-1), vascular cell adhesion molecule-1 (VCAM-1), and endothelial leukocyte adhesion molecule (ELAM-1) by endothelial cells. J Invest Dermatol. 1993; 100(6):759–765. [PubMed: 7684425]
17. Klein CL, Nieder P, Wagner M, Köhler H, Bittinger F, Kirkpatrick CJ, Lewis JC. The role of metal corrosion in inflammatory processes: induction of adhesion molecules by heavy metal ions. J Mater Sci - Mater Med. 1994; 5(11):798–807.

18. Goebeler M, Roth J, Bröcker EB, Sorg C, Schulze-Osthoff K. Activation of nuclear factor-kappa B and gene expression in human endothelial cells by the common haptens nickel and cobalt. J Immunol. 1995; 155(5):2459–2467. [PubMed: 7544377]
19. Wagner M, Klein CL, Kleinert H, Euchenhofer C, Förstermann U, Kirkpatrick CJ. Heavy metal ion induction of adhesion molecules and cytokines in human endothelial cells: the role of NF-κB, lκB-α and AP-1. Pathobiology. 1997; 65(5):241–252. [PubMed: 9459494]
20. Wagner M, Klein CL, van Kooten TG, Kirkpatrick CJ. Mechanisms of cell activation by heavy metal ions. J Biomed Mater Res. 1998; 42(3):443–452. [PubMed: 9788508]
21. Messer RLW, Wataha JC, Lewis JB, Lockwood PE, Caughman GB, Tseng W-Y. Effect of vascular stent alloys on expression of cellular adhesion molecules by endothelial cells. J Long Term Eff Med Implants. 2005; 15(1):39–48. [PubMed: 15715515]
22. Martinesi M, Bruni S, Stio M, Treves C, Borgioli F. In vitro interaction between surface-treated Ti-6Al-4V titanium alloy and human peripheral blood mononuclear cells. J Biomed Mater Res, Part A. 2005; 74A(2):197– 207.
23. McLucas E, Rochev Y, Carroll WM, Smith TJ. Analysis of the effects of surface treatments on nickel release from nitinol wires and their impact on candidate gene expression in endothelial cells. J Mater Sci - Mater Med. 2008; 19(3):975–980. [PubMed: 18250966]
24. Cybulsky MI, Iiyama K, Li H, Zhu S, Chen M, Iiyama M, Davis V, Gutierrez-Ramos J-C, Connelly PW, Milstone DS. A major role for VCAM-1, but not ICAM-1, in early atherosclerosis. J Clin Invest. 2001; 107(10):1255– 1262. [PubMed: 11375415]
25. Bayata S, Arikan E, Yesil M, Postaci N, Tas A, Koseoglu M. An important role for VCAM-1, but not for ICAM-1 in restenosis following coronary implantation. Anadolu Kardiyoloji Dergisi. 2010; 10(5):405–409. [PubMed: 20929696]
26. Guan RG, Cipriano AF, Zhao ZY, Lock J, Tie D, Zhao T, Cui T, Liu H. Development and evaluation of a magnesium-zinc-strontium alloy for biomedical applications – alloy processing. Microstruct Mech Prop Biodegrad Mater Sci Eng C. 2013; 33(7):3661–3669.
27. Cipriano AF, Zhao T, Johnson I, Guan R-G, Garcia S, Liu H. In vitro degradation of four magnesium–zinc–strontium alloys and their cytocompatibility with human embryonic stem cells. J Mater Sci - Mater Med. 2013; 24(4):989–1003. [PubMed: 23361966]
28. Nguyen TY, Cipriano AF, Guan RG, Zhao ZY, Liu H. In vitro interactions of blood, platelet, and fibroblast with biodegradable Magnesium-Zinc-Strontium alloys. J Biomed Mater Res, Part A. 2015; 103(9):2974–2986.
29. Cipriano AF, Sallee A, Guan R-G, Zhao Z-Y, Tayoba M, Sanchez J, Liu H. Investigation of magnesium–zinc–calcium alloys and bone marrow derived mesenchymal stem cell response in direct culture. Acta Biomater. 2015; 12(1):298–321. [PubMed: 25449917]
30. Fischer J, Pröfrock D, Hort N, Willumeit R, Feyerabend F. Reprint of: Improved cytotoxicity testing of magnesium materials. Mater Sci Eng, B. 2011; 176(20):1773–1777.
31. Wang J, Witte F, Xi T, Zheng Y, Yang K, Yang Y, Zhao D, Meng J, Li Y, Li W, Chan K, Qin L. Recommendation for modifying current cytotoxicity testing standards for biodegradable magnesium-based materials. Acta Biomater. 2015; 21:237–249. [PubMed: 25890098]
32. Jung O, Smeets R, Porchetta D, Kopp A, Ptock C, Müller U, Heiland M, Schwade M, Behr B, Kröger N, Kluwe L, Hanken H, Hartjen P. Optimized in vitro procedure for assessing the cytocompatibility of magnesium-based biomaterials. Acta Biomater. 2015; 23:354–363. [PubMed: 26073090]
33. Witte F, Ulrich H, Rudert M, Willbold E. Biodegradable magnesium scaffolds: Part 1: appropriate inflammatory response. J Biomed Mater Res, Part A. 2007; 81A(3):748–756.
34. Willbold E, Kaya AA, Kaya RA, Beckmann F, Witte F. Corrosion of magnesium alloy AZ31 screws is dependent on the implantation site. Mater Sci Eng, B. 2011; 176(20):1835–1840.
35. Bondarenko A, Hewicker-Trautwein M, Erdmann N, Angrisani N, Reifenrath J, Meyer-Lindenberg A. Comparison of morphological changes in efferent lymph nodes after implantation of resorbable and non-resorbable implants in rabbits. BioMed Eng OnLine. 2011; 10(32):1–15. [PubMed: 21244718]

36. Kraus T, Fischerauer SF, Hänzi AC, Uggowitzer PJ, Löffler JF, Weinberg AM. Magnesium alloys for temporary implants in osteosynthesis: in vivo studies of their degradation and interaction with bone. Acta Biomater. 2012; 8(3):1230–1238. [PubMed: 22107870]
37. Badar M, Lünsdorf H, Evertz F, Rahim MI, Glasmacher B, Hauser H, Mueller PP. The formation of an organic coat and the release of corrosion microparticles from metallic magnesium implants. Acta Biomater. 2013; 9(7):7580–7589. [PubMed: 23518475]
38. Roth I, Schumacher S, Basler T, Baumert K, Seitz J-M, Evertz F, Müller P, Bäumer W, Kietzmann M. Magnesium corrosion particles do not interfere with the immune function of primary human and murine macrophages. Prog Biomater. 2014:1–10. [PubMed: 29470791]
39. Feser K, Kietzmann M, Bäumer W, Krause C, Bach FW. Effects of degradable Mg-Ca alloys on dendritic cell function. J Biomater Appl. 2011; 25(7):685– 697. [PubMed: 20207778]
40. Witte F, Kaese V, Haferkamp H, Switzer E, Meyer-Lindenberg A, Wirth CJ, Windhagen H. In vivo corrosion of four magnesium alloys and the associated bone response. Biomaterials. 2005; 26(17): 3557–3563. [PubMed: 15621246]
41. Gu XN, Zheng YF, Chen LJ. Influence of artificial biological fluid composition on the biocorrosion of potential orthopedic Mg-Ca, AZ31, AZ91 alloys. Biomed Mater. 2009; 4(6): 065011. [PubMed: 19966381]
42. Zhang X, Yuan G, Mao L, Niu J, Ding W. Biocorrosion properties of as-extruded Mg–Nd–Zn–Zr alloy compared with commercial AZ31 and WE43 alloys. Mater Lett. 2012; 66(1):209–211.
43. Mani G, Feldman MD, Patel D, Agrawal CM. Coronary stents: a materials perspective. Biomaterials. 2007; 28(9):1689–1710. [PubMed: 17188349]
44. Moravej M, Mantovani D. Biodegradable metals for cardiovascular stent application: interests and new opportunities. Int J Mol Sci. 2011; 12(7):4250–4270. [PubMed: 21845076]
45. Iskandar ME, Aslani A, Liu H. The effects of nanostructured hydroxyapatite coating on the biodegradation and cytocompatibility of magnesium implants. J Biomed Mater Res, Part A. 2013; 101A(8):2340–2354.
46. Potapova TA, Sivakumar S, Flynn JN, Li R, Gorbsky GJ. Mitotic progression becomes irreversible in prometaphase and collapses when Wee1 and Cdc25 are inhibited. Mol Biol Cell. 2011; 22(8): 1191–1206. [PubMed: 21325631]
47. Nguyen TY, Liew CG, Liu H. An in vitro mechanism study on the proliferation and pluripotency of human embryonic stems cells in response to magnesium degradation. PLoS ONE. 2013; 8(10):e76547. [PubMed: 24146887]
48. Kirkland NT, Birbilis N, Staiger MP. Assessing the corrosion of biodegradable magnesium implants: a critical review of current methodologies and their limitations. Acta Biomater. 2012; 8(3):925–936. [PubMed: 22134164]
49. Kelly, RG., Scully, JR., Shoesmith, D., Buchheit, RG. Electrochemical Techniques in Corrosion Science and Engineering. CRC Press; 2002.
50. Dubin-Thaler BJ, Giannone G, Döbereiner H-G, Sheetz MP. Nanometer analysis of cell spreading on matrix-coated surfaces reveals two distinct cell states and STEPs. Biophys J. 2004; 86(3):1794–1806. [PubMed: 14990505]
51. Knedler A, Ham R. Optimized medium for clonal growth of human microvascular endothelial cells with minimal serum. Vitro Cell Dev Biol. 1987; 23(7):481–491.
52. Brar HS, Wong J, Manuel MV. Investigation of the mechanical and degradation properties of Mg–Sr and Mg–Zn–Sr alloys for use as potential biodegradable implant materials. J Mech Behav Biomed Mater. 2012; 7:87–95. [PubMed: 22340688]
53. Li H, Peng Q, Li X, Li K, Han Z, Fang D. Microstructures, mechanical and cytocompatibility of degradable Mg–Zn based orthopedic biomaterials. Mater Des. 2014; 58:43–51.
54. Aljarrah M, Aghaulor U, Medraj M. Thermodynamic assessment of the Mg–Zn–Sr system. Intermetallics. 2007; 15(2):93–97.
55. Cui T, Guan R-G, Qin H-M. The microstructure and the degradation behaviour of a novel biomaterial Mg-Zn-Sr alloy sheet in simulated body fluid (SBF). Adv Sci Lett. 2013; 19(4):1082–1085.

56. Xia X, Davies CHJ, Nie JF, Birbilis N. Influence of composition and processing on the corrosion of magnesium alloys containing binary and ternary additions of zinc and strontium. Corrosion. 2014; 71(1):38–49.
57. Niinomi M. Recent metallic materials for biomedical applications. Metal Mater Trans A. 2002; 33(3):477–486.
58. Alvarez-Lopez M, Pereda MD, del Valle JA, Fernandez-Lorenzo M, Garcia-Alonso MC, Ruano OA, Escudero ML. Corrosion behaviour of AZ31 magnesium alloy with different grain sizes in simulated biological fluids. Acta Biomater. 2010; 6(5):1763–1771. [PubMed: 19446048]
59. Haiwei L, Ke X, Ke Y, Jing L, Binchun Z, Yonghui X, Feng Z, Hongbo H, Lili T, Duo H. The degradation performance of AZ31 bioabsorbable magnesium alloy stent implanted in the abdominal aorta of rabbits. J Interventional Radiol Chin. 2010; 19(4):315–317.
60. Zhang, BP., Wang, Y., Geng, L. Research on Mg-Zn-Ca alloy as degradable biomaterial. In: Pignatello, R., editor. Biomaterials – Physics and Chemistry. InTech; Rijeka, Croatia: 2011. p. 183-204.
61. Cha P-R, Han H-S, Yang G-F, Kim Y-C, Hong K-H, Lee S-C, Jung J-Y, Ahn J-P, Kim Y-Y, Cho S-Y, Byun JY, Lee K-S, Yang S-J, Seok H-K. Biodegradability engineering of biodegradable Mg alloys: tailoring the electrochemical properties and microstructure of constituent phases. Sci Rep. 2013; 3
62. Hänzi AC, Gerber I, Schinhammer M, Löffler JF, Uggowitzer PJ. On the in vitro and in vivo degradation performance and biological response of new biodegradable Mg–Y–Zn alloys. Acta Biomater. 2010; 6(5):1824–1833. [PubMed: 19815099]
63. Huan ZG, Leeflang MA, Zhou J, Fratila-Apachitei LE, Duszczyk J. In vitro degradation behavior and cytocompatibility of Mg–Zn–Zr alloys. J Mater Sci - Mater Med. 2010; 21(9):2623–2635. [PubMed: 20532960]
64. Zhang E, Yin D, Xu L, Yang L, Yang K. Microstructure, mechanical and corrosion properties and biocompatibility of Mg–Zn–Mn alloys for biomedical application. Mater Sci Eng, C. 2009; 29(3): 987–993.
65. Rosalbino F, Negri S, Saccone A, Angelini E, Delfino S. Bio-corrosion characterization of Mg–Zn–X (X = Ca, Mn, Si) alloys for biomedical applications. J Mater Sci - Mater Med. 2010; 21(4): 1091–1098. [PubMed: 20020186]
66. Persaud-Sharma D, Budiansky N. In vitro degradation behavior of ternary Mg-Zn-Se and Mg-Zn-Cu alloys as biomaterials. J Biomimetics Biomater Tissue Eng. 2013; 18(1)
67. Liu L, Li N, Lei T, Li K, Zhang Y. The in vitro biological properties of Mg-Zn-Sr alloy and superiority for preparation of biodegradable intestinal anastomosis rings. Med Sci Monitor. 2014; 20:1056–1066.
68. Liu H. The effects of surface and biomolecules on magnesium degradation and mesenchymal stem cell adhesion. J Biomed Mater Res A. 2011; 99(2):249–260. [PubMed: 21976450]
69. Johnson I, Perchy D, Liu H. In vitro evaluation of the surface effects on magnesium-yttrium alloy degradation and mesenchymal stem cell adhesion. J Biomed Mater Res A. 2011; 100A(2):477–485.
70. Sands JM, Layton HE. The physiology of urinary concentration: an update. Semin Nephrol. 2009; 29(3):178–195. [PubMed: 19523568]
71. Zhao N, Zhu D. Endothelial responses of magnesium and other alloying elements in magnesium-based stent materials. Metallomics. 2015; 7(1):118–128. [PubMed: 25363018]
72. Lelong IH, Rebel G. Ph drift of “physiological buffers” and culture media used for cell incubation during in vitro studies. J Pharmacol Toxicol Methods. 1998; 39(4):203–210. [PubMed: 9845299]
73. Romani A. Regulation of magnesium homeostasis and transport in mammalian cells. Arch Biochem Biophys. 2007; 458(1):90–102. [PubMed: 16949548]
74. Maier JAM, Bernardini D, Rayssiguier Y, Mazur A. High concentrations of magnesium modulate vascular endothelial cell behaviour in vitro. Biochim Biophys Acta. 2004; 1689(1):6–12. [PubMed: 15158908]
75. Maier JAM, Malpuech-Brugère C, Zimowska W, Rayssiguier Y, Mazur A. Low magnesium promotes endothelial cell dysfunction: implications for atherosclerosis, inflammation and thrombosis. Biochim Biophys Acta. 2004; 1689(1):13–21. [PubMed: 15158909]

76. Yang C, Yuan G, Zhang J, Tang Z, Zhang X, Dai K. Effects of magnesium alloys extracts on adult human bone marrow-derived stromal cell viability and osteogenic differentiation. Biomed Mater. 2010; 5(4):045005. [PubMed: 20571183]
77. Grillo CA, Alvarez F, Fernández MA. Lorenzo de Mele, biological effects of magnesium particles degradation on UMR-106 cell line: influence of fluoride treatments. Colloids Surf, B. 2011; 88(1): 471–476.
78. Pober JS, Bevilacqua MP, Mendrick DL, Lapierre LA, Fiers W, Gimbrone MA. Two distinct monokines, interleukin 1 and tumor necrosis factor, each independently induce biosynthesis and transient expression of the same antigen on the surface of cultured human vascular endothelial cells. J Immunol. 1986; 136(5):1680–1687. [PubMed: 3485132]
79. Pober JS, Gimbrone MA, Lapierre LA, Mendrick DL, Fiers W, Rothlein R, Springer TA. Overlapping patterns of activation of human endothelial cells by interleukin 1, tumor necrosis factor, and immune interferon. J Immunol. 1986; 137(6):1893–1896. [PubMed: 3091693]
80. Leeuwenberg JF, Smeets EF, Neefjes JJ, Shaffer MA, Cinek T, Jeunhomme TM, Ahern TJ, Buurman WA. E-selectin and intercellular adhesion molecule-1 are released by activated human endothelial cells in vitro. Immunology. 1992; 77(4):543–549. [PubMed: 1283598]
81. Osborn L, Hession C, Tizard R, Vassallo C, Luhowskyj S, Chi-Rosso G, Lobb R. Direct expression cloning of vascular cell adhesion molecule 1, a cytokine-induced endothelial protein that binds to lymphocytes. Cell. 1989; 59(6):1203–1211. [PubMed: 2688898]
82. Zhang W-J, Frei B. Intracellular metal ion chelators inhibit TNFα-induced SP-1 activation and adhesion molecule expression in human aortic endothelial cells. Free Radical Biol Med. 2003; 34(6):674–682. [PubMed: 12633744]
83. Rochelson B, Dowling O, Schwartz N, Metz CN. Magnesium sulfate suppresses inflammatory responses by human umbilical vein endothelial cells (HuVECs) through the NFκB pathway. J Reprod Immunol. 2007; 73(2):101–107. [PubMed: 16952401]
84. Zhai Z, Qu X, Li H, Yang K, Wan P, Tan L, Ouyang Z, Liu X, Tian B, Xiao F, Wang W, Jiang C, Tang T, Fan Q, Qin A, Dai K. The effect of metallic magnesium degradation products on osteoclast-induced osteolysis and attenuation of NF-κB and NFATc1 signaling. Biomaterials. 2014; 35(24):6299–6310. [PubMed: 24816285]
85. Prasad AS, Bao B, Beck FWJ, Sarkar FH. Zinc activates NF-κB in HUT-78 cells. J Lab Clin Med. 2001; 138(4):250–256. [PubMed: 11574819]
86. Bao B, Prasad AS, Beck FWJ, Sarkar FH. Zinc up-regulates NF-κB activation via phosphorylation of IκB in HUT-78 (Th0) cells. FEBS Lett. 2007; 581(23):4507–4511. [PubMed: 17765898]
87. Strlič M, Kolar J, Šelih V-S, Kočar D, Pihlar B. A comparative study of several transition metals in Fenton-like reaction systems at circum-neutral pH. Acta Chim Slov. 2003; 50(4):619–632.
88. Wilham, JM. Biomedical and Pharmaceutical Sciences. University of Montana; 2007. The Role of Zinc and Reactive Oxygen Species in the Regulation of Endothelial Nitric Oxide Synthase; p. 190
89. Cortese-Krott MM, Kulakov L, Opländer C, Kolb-Bachofen V, Kröncke K-D, Suschek CV. Zinc regulates iNOS-derived nitric oxide formation in endothelial cells. Redox Biol. 2014; 2:945–954. [PubMed: 25180171]
90. Kocatürk P, Kavas G, Erdeve Ö, Siklar Z. Superoxide dismutase activity and zinc and copper concentrations in growth retardation. Biol Trace Elem Res. 2004; 102(1–3):51–59. [PubMed: 15621927]
91. Khan BV, Harrison DG, Olbrych MT, Alexander RW, Medford RM. Nitric oxide regulates vascular cell adhesion molecule 1 gene expression and redox-sensitive transcriptional events in human vascular endothelial cells. Proc Natl Acad Sci. 1996; 93(17):9114–9119. [PubMed: 8799163]
92. Lin S-J, Shyue S-K, Hung Y-Y, Chen Y-H, Ku H-H, Chen J-W, Tam K-B, Chen Y-L. Superoxide dismutase inhibits the expression of vascular cell adhesion molecule-1 and intracellular cell adhesion molecule-1 induced by tumor necrosis factor-α in human endothelial cells through the JNK/p38 pathways. Arterioscler Thromb Vasc Biol. 2005; 25(2):334–340. [PubMed: 15576639]
93. Prasad AS. Clinical, immunological, anti-inflammatory and antioxidant roles of zinc. Exp Gerontol. 2008; 43(5):370–377. [PubMed: 18054190]
94. Prasad AS. Zinc: role in immunity, oxidative stress and chronic inflammation. Curr Opin Clin Nutr Metabol Care. 2009; 12(6):646–652.

95. Prasad AS. Zinc: an antioxidant and anti-inflammatory agent: role of zinc in degenerative disorders of aging. J Trace Elem Med Biol. 2014; 28(4):364–371. [PubMed: 25200490]

96. Xu L, Yu G, Zhang E, Pan F, Yang K. In vivo corrosion behavior of Mg-Mn-Zn alloy for bone implant application. J Biomed Mater Res, Part A. 2007; 83A(3):703–711.

97. Zhang E, Xu L, Yu G, Pan F, Yang K. In vivo evaluation of biodegradable magnesium alloy bone implant in the first 6 months implantation. J Biomed Mater Res, Part A. 2009; 90(3):882–893.

98. Xu L, Pan F, Yu G, Yang L, Zhang E, Yang K. In vitro and in vivo evaluation of the surface bioactivity of a calcium phosphate coated magnesium alloy. Biomaterials. 2009; 30(8):1512–1523. [PubMed: 19111896]

99. Klein CL, Köhler H, Kirkpatrick CJ. Increased adhesion and activation of polymorphonuclear neutrophil granulocytes to endothelial cells under heavy metal exposure in vitro. Pathobiology. 1994; 62(2):90–98. [PubMed: 7524527]

100. Arsalane K, Gosset P, Hildebrand HF, Voisin C, Tonnel A-B, Wallaert B. Nickel hydroxy carbonate increases tumour necrosis factor alpha and interleukin 6 secretion by alveolar macrophages. J Appl Toxicol. 1994; 14(5):375–379. [PubMed: 7822688]

101. Ninomiya JT, Kuzma SA, Schnettler TJ, Krolikowski JG, Struve JA, Weihrauch D. Metal ions activate vascular endothelial cells and increase lymphocyte chemotaxis and binding. J Orthop Res. 2013; 31(9):1484– 1491. [PubMed: 23629852]

102. Liu H, Webster TJ. Nanomedicine for implants: a review of studies and necessary experimental tools. Biomaterials. 2007; 28(2):354–369. [PubMed: 21898921]

103. Chung T-W, Liu D-Z, Wang S-Y, Wang S-S. Enhancement of the growth of human endothelial cells by surface roughness at nanometer scale. Biomaterials. 2003; 24(25):4655–4661. [PubMed: 12951008]

104. Franco D, Klingauf M, Bednarzik M, Cecchini M, Kurtcuoglu V, Gobrecht J, Poulikakos D, Ferrari A. Control of initial endothelial spreading by topographic activation of focal adhesion kinase. Soft Matter. 2011; 7(16):7313–7324.

105. Liliensiek SJ, Wood JA, Yong J, Auerbach R, Nealey PF, Murphy CJ. Modulation of human vascular endothelial cell behaviors by nanotopographic cues. Biomaterials. 2010; 31(20):5418–5426. [PubMed: 20400175]

106. Bowen PK, Drelich J, Goldman J. Magnesium in the murine artery: probing the products of corrosion. Acta Biomater. 2014; 10(3):1475–1483. [PubMed: 24296127]

107. Ruygrok PN, Serruys PW. Intracoronary stenting: from concept to custom. Circulation. 1996; 94(5):882–890. [PubMed: 8790021]

Statement of Significance

Magnesium (Mg) alloys specifically designed for biodegradable implant applications have been the focus of biomedical research since the early 2000s. Physicochemical properties of Mg alloys make these metallic biomaterials excellent candidates for temporary biodegradable implants in orthopedic and cardiovascular applications. As Mg alloys continue to be investigated for biomedical applications, it is necessary to understand whether Mg-based materials or the alloying elements have the intrinsic ability to direct an immune response to improve implant integration while avoiding cell-biomaterial interactions leading to chronic inflammation and/or foreign body reactions. The present study utilized the direct culture method to investigate for the first time the *in vitro* transient inflammatory activation of endothelial cells induced by the degradation products of Zn-containing Mg alloys.

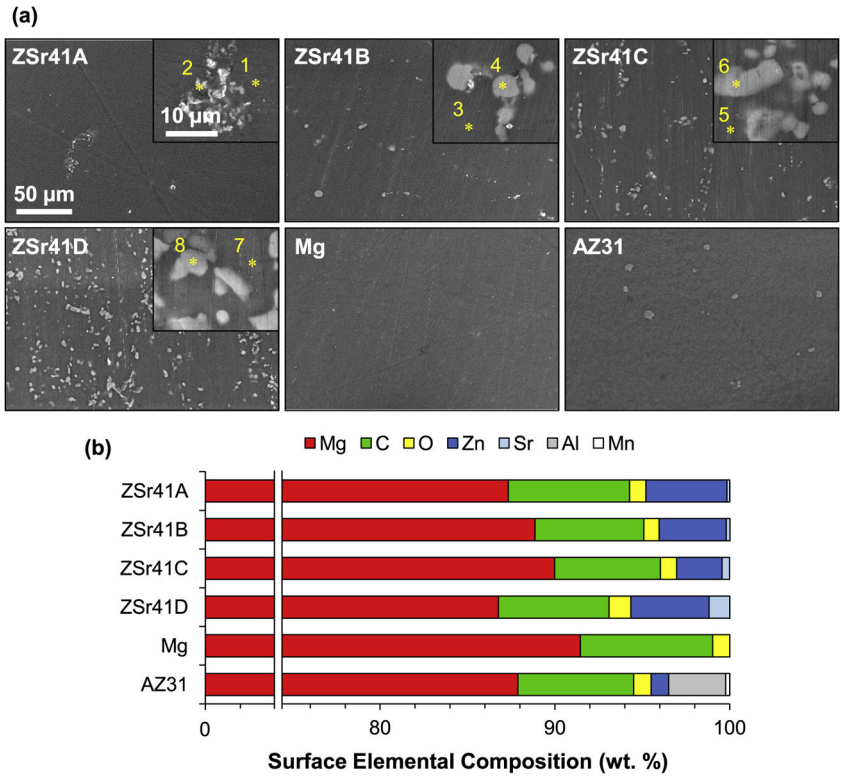

Fig. 1.

Microstructural analyses of ZSr41 alloys. (a) SEM images of ZSr41A-D alloys, commercial pure Mg (control), and commercial AZ31 alloy (reference). Scale bar = 50 µm for all images. Original magnification: 600×. Insets in (a) are SEM images of the secondary phases respective to each alloy at a high magnification of 5000×. Scale bar = 10 µm for all insets. (b) Surface elemental composition (wt%) quantified through EDS area analysis on (a) at 600× magnification. Points 1–8 represent locations for the EDS point analyses for which results are shown in Fig. 2.

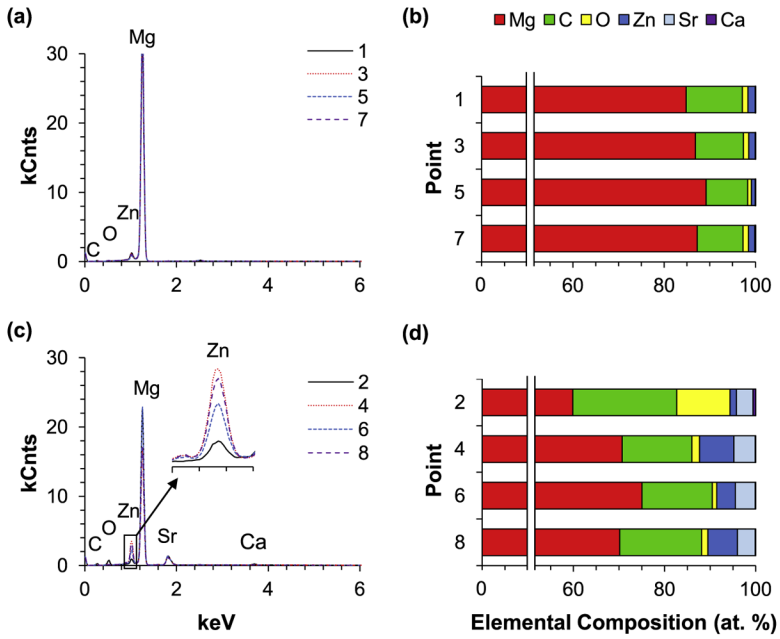

Fig. 2.

EDS analyses of the primary and secondary phases of ZSr41 alloys, including (a,c) EDS spectra and (b,d) quantification of elemental composition (at%). (a) and (b): EDS analyses of points 1, 3, 5, and 7 at the α-matrices of ZSr41A-D in Fig. 1a; (c) and (d): EDS analyses of points 2, 4, 6, and 8 at the intermetallic β-phases in ZSr41A-D in Fig. 1a.

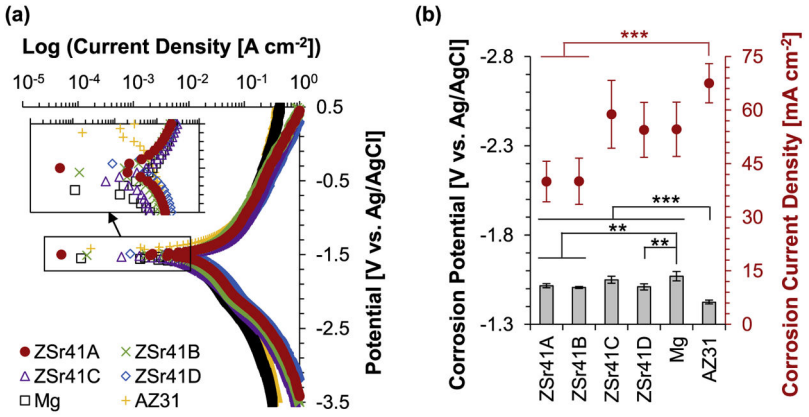

Fig. 3.

Electrochemical testing results of ZSr41 alloys, pure Mg control, and AZ31 reference. (a) potentiodynamic polarization curves of the polished Mg-based samples at 37 °C using r-SBF as the electrolyte; and (b) corrosion potential and corrosion current density of ZSr41 alloys, pure Mg, and AZ31 obtained from Tafel extrapolation (ASTM G102-89) of potentiodynamic polarization curves; values are mean ± SD, n = 3, $^{**}p < 0.01$, $^{***}p < 0.001$.

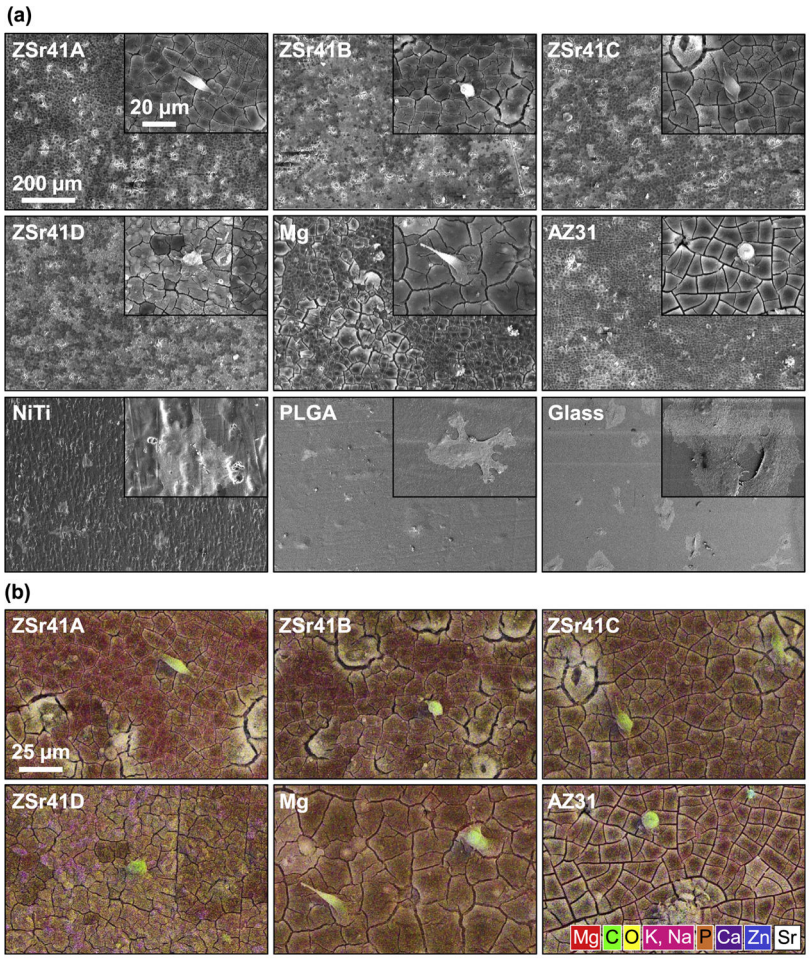

Fig. 4.

Human umbilical vein endothelial cells (HUVECs) in direct contact with ZSr41 alloy surface after 4 h of direct culture in EGM™-2 media. (a) SEM micrographs of ZSr41 alloys, pure Mg (control), and reference materials (AZ31 alloy, NiTi, PLGA, and glass, respectively). Original magnification: 150×; scale bar = 200 μm for all images. Insets in (a) were taken at 1000× original magnification with scale bar = 20 μm for all images. (b) SEM-EDS composite image of the ZSr41 alloys, Mg control, and AZ31 reference at 1000× magnification. The color mapping in each image represents surface elemental distribution measured by EDS (red = Mg, green = C, yellow = O, pink = K, Na, orange = P, purple = Ca, blue = Zn, white = Sr). Scale bar = 25 μm for all images. (For interpretation of the references to colour in this figure legend, the reader is referred to the web version of this article.)

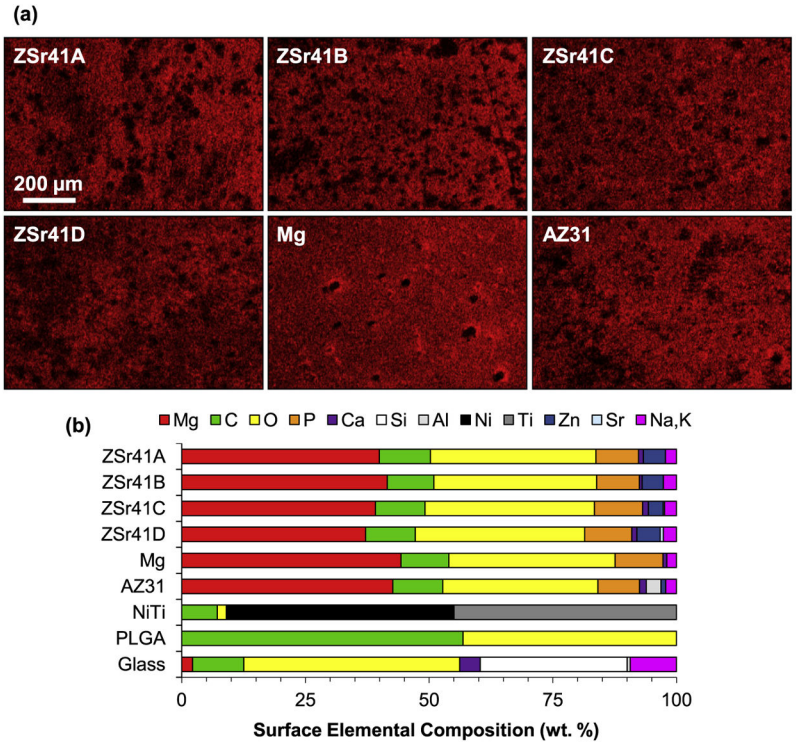

Fig. 5.

Surface characterization of Mg-based materials: (a) EDS elemental distribution map of Mg Kα1 lines of ZSr41 alloys (A–D), pure Mg (control), and AZ31 alloy (reference), respectively, after 4 h direct culture with HUVECs in EGM™-2 media. Original magnification: 150×; scale bar = 200 μm for all images. (b) Surface elemental composition (wt%) based on EDS quantification on 150× images of Mg-based materials, NiTi, PLGA, and glass.

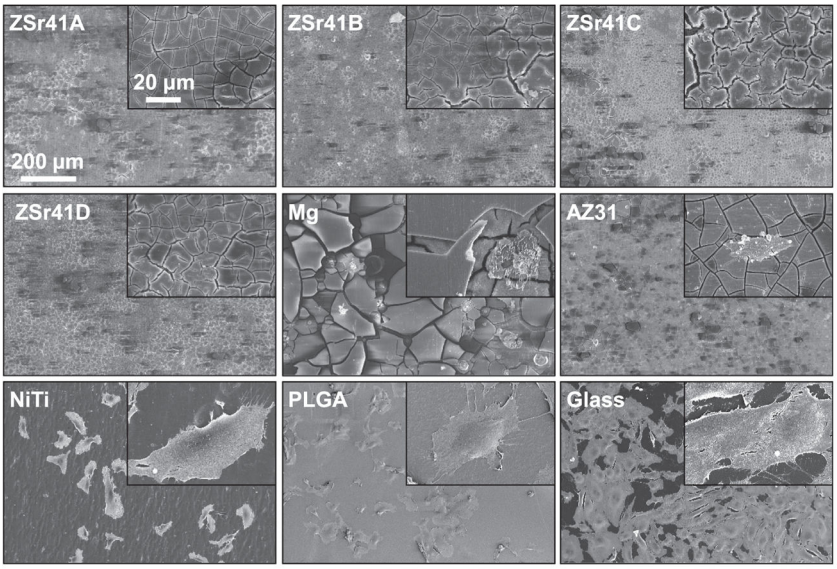

Fig. 6.

HUVECs in direct contact with ZSr41 alloy surface after 24 h of direct culture in EGM™-2 media. SEM micrographs of ZSr41 alloys, pure Mg (control), and reference materials (AZ31 alloy, NiTi, PLGA, and glass, respectively). Original magnification: 150×; scale bar = 200 μm for all images. Insets in were taken at 1000× original magnification with scale bar = 20 μm for all images.

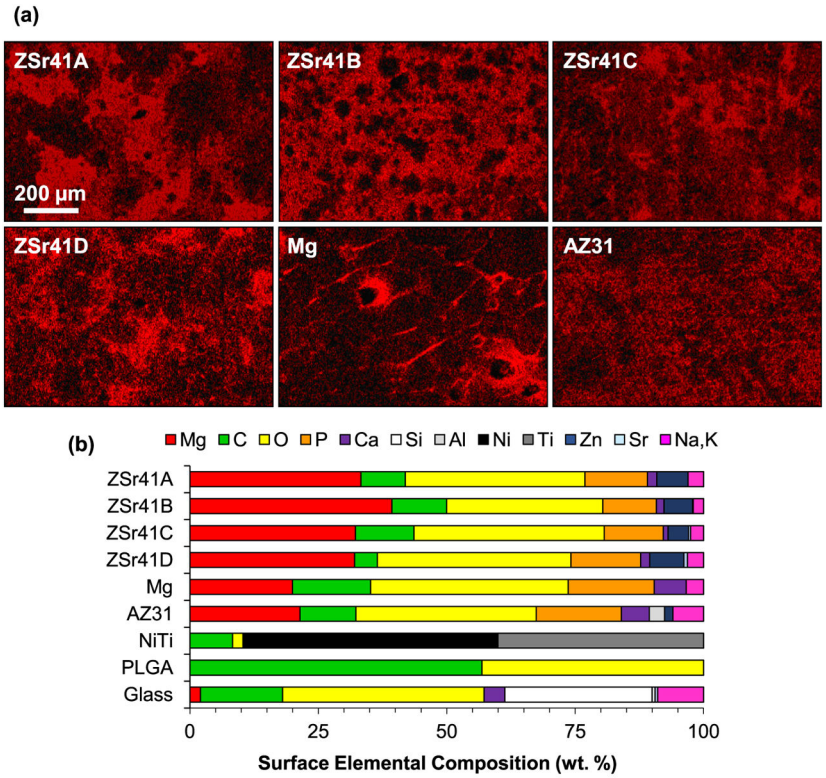

Fig. 7.

Surface characterization of Mg-based materials: (a) EDS elemental distribution map of Mg Kα1 lines of ZSr41 alloys (A–D), pure Mg (control), and AZ31 alloy (reference), respectively, after 24 h direct culture with HUVECs in EGM™-2 media. Original magnification: 150×; scale bar = 200 μm for all images. (b) Surface elemental composition (wt%) based on EDS quantification on 150× images of Mg-based materials, NiTi, PLGA, and glass.

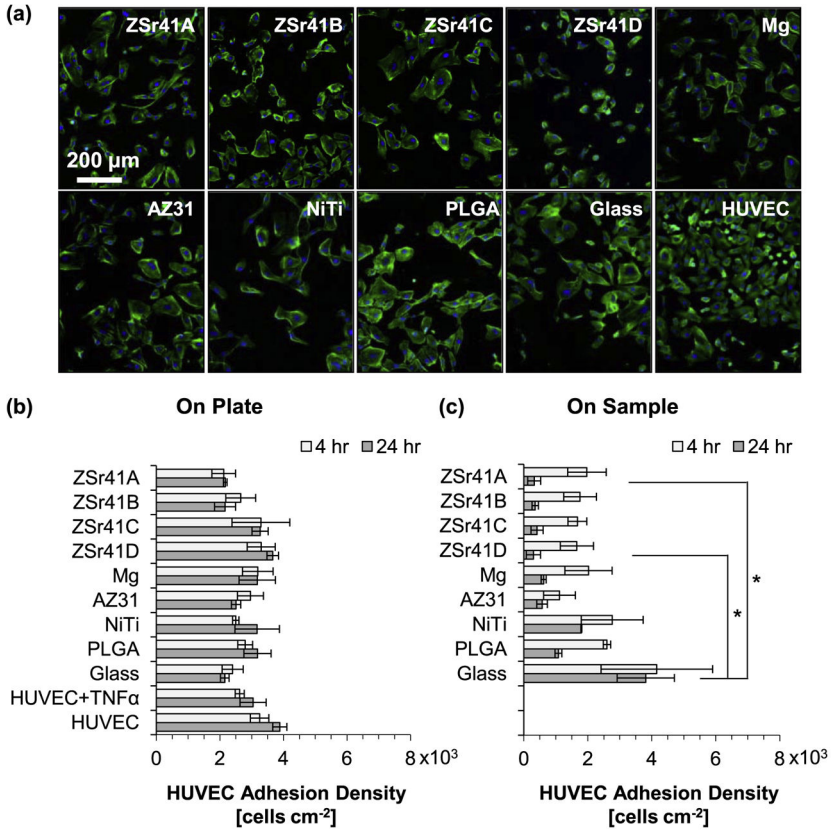

Fig. 8.

HUVEC adhesion after 4 and 24 h of direct culture on ZSr41 alloys (A–D), pure Mg control, reference materials (AZ31 alloy, NiTi, PLGA, and glass), cells only supplemented with 10 ng/mL TNFα, and cells only control: (a) representative fluorescence images of adhered HUVECs at 24 h on the tissue culture plates, (b) adhesion density on the culture plate surrounding each corresponding sample (indirect contact with the sample), and (c) adhesion density on the sample surface (direct contact with the sample). Values are mean ± standard error of the means, n = 3; $^{*}p < 0.05$.

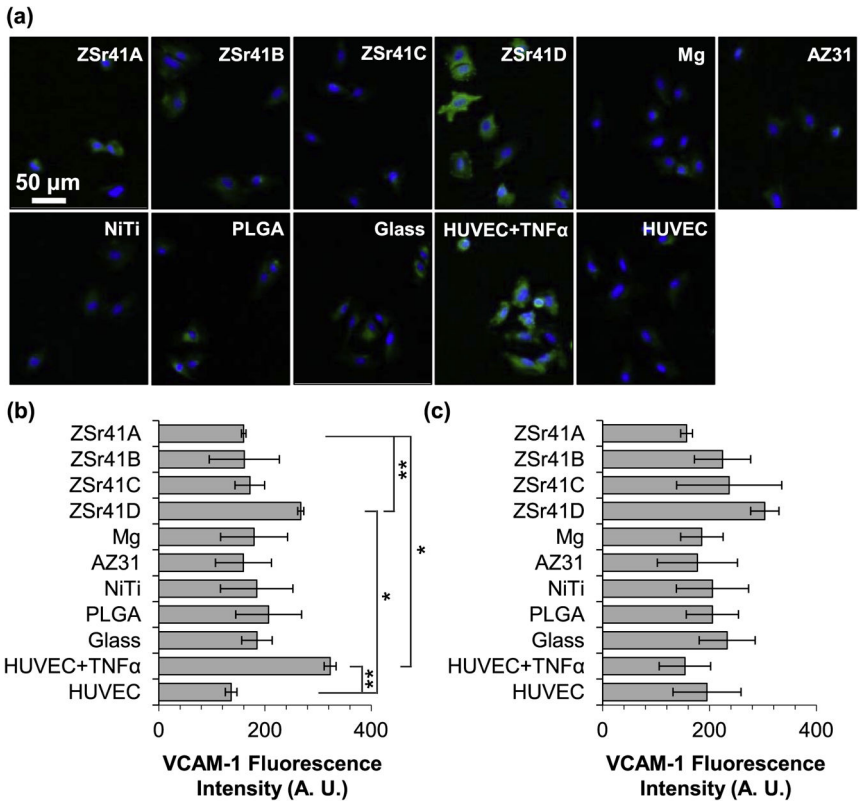

Fig. 9.

HUVEC responses after 4 and 24 h of direct culture with ZSr41 alloys (A–D), pure Mg control, reference materials (AZ31 alloy, NiTi, PLGA, and glass), cells only supplemented with 10 ng/mL TNFα (positive control), and cells only (negative control): (a) Fluorescence images of adhered HUVECs at 4 h culture. Blue color indicates DAPI stained nuclei and green color indicates FITC-labeled VCAM-1. Scale bar = 50 μm for all images. (b) Quantification of VCAM-1 mean fluorescence intensity signal per pixel at 4 h culture. (c) Quantification of VCAM-1 mean fluorescence intensity signal per pixel at 24 h culture. All results were only for cells adhered on the culture plate surrounding the samples. Values are mean ± SEM, n = 3, $^{*}p < 0.05$ and $^{**}p < 0.01$.

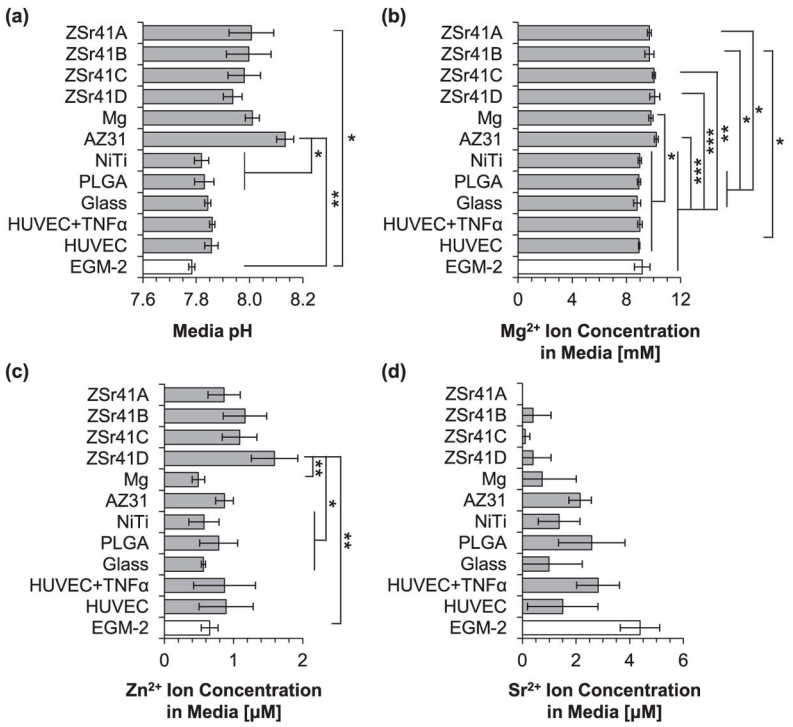

Fig. 10.

Analysis of solubilized degradation products in culture media after 4 h of direct culture with ZSr41 alloys (A–D), pure Mg control, reference materials (AZ31 alloy, NiTi, PLGA, and glass), cells only supplemented with 10 ng/mL TNFα, cells only, and blank EGM™-2 media: (a) pH of media, (b) Mg^{2+} ion concentration, (c) Zn^{2+} ion concentration, and (d) Sr^{2+} ion concentration. Values are mean ± SD, n = 3. $^{*}p < 0.05$, $^{**}p < 0.01$, $^{***}p < 0.001$.

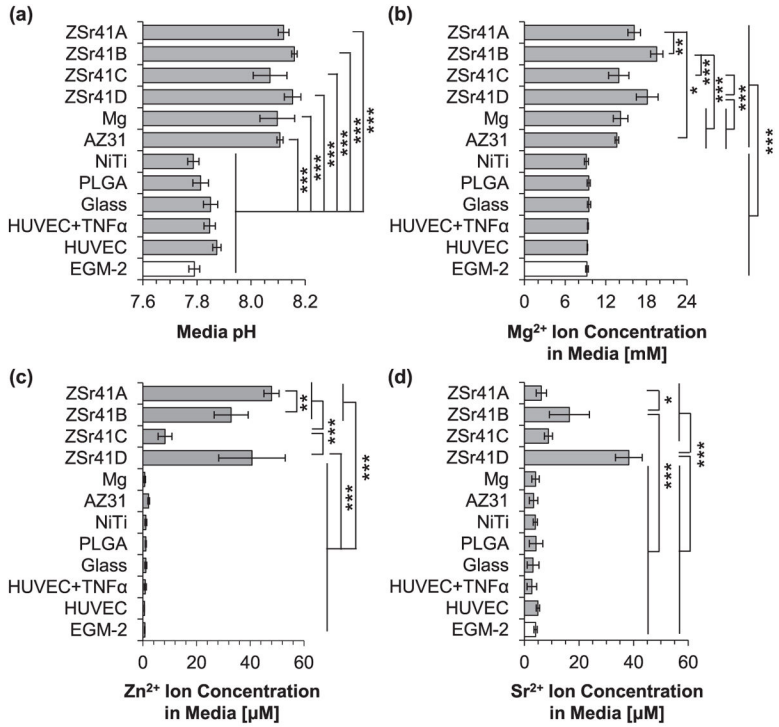

Fig. 11.

Analysis of solubilized degradation products in culture media after 24 h of direct culture with ZSr41 alloys (A–D), pure Mg control, reference materials (AZ31 alloy, NiTi, PLGA, and glass), cells only supplemented with 10 ng/mL TNFα, cells only, and blank EGM™-2 media: (a) pH of media, (b) Mg^{2+} ion concentration, (c) Zn^{2+} ion concentration, and (d) Sr^{2+} ion concentration. Values are mean ± SD, n = 3. $^{*}p < 0.05$, $^{**}p < 0.01$, $^{***}p < 0.001$.

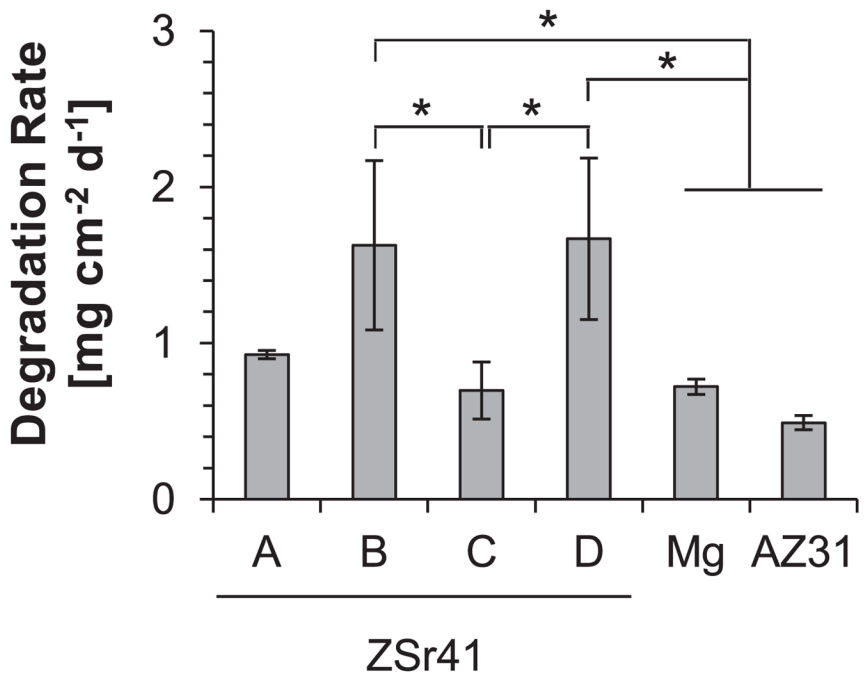

Fig. 12.

Average daily degradation rate (mass loss rate) per unit surface area of ZSr41 alloys, pure Mg control, and AZ31 reference in EGM™-2 culture media during 24 h of incubation. Values are mean ± SD, n = 3; $^{*}p < 0.05$.

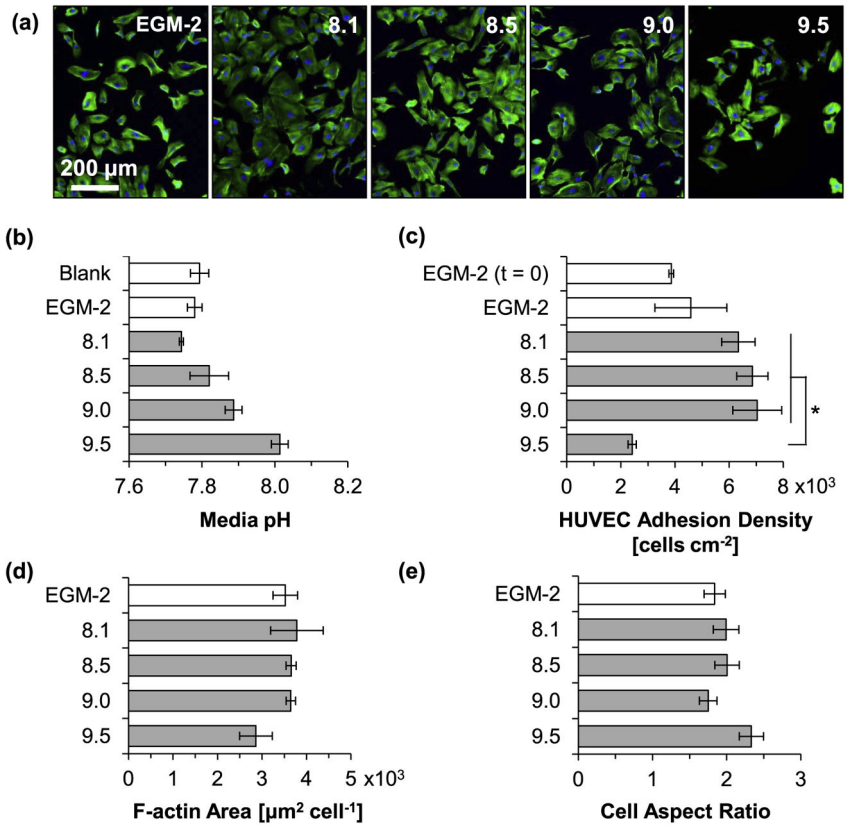

Fig. 13.

HUVEC behaviors after 24 h of incubation in complete EGM™-2 media with initial pH values intentionally adjusted to 8.1–9.5. (a) Fluorescence images of HUVECs. Blue color indicates DAPI stained nuclei and green color indicates Alexa Fluor® 488 stained F-actin (cytoskeleton). Scale bar = 200 µm for all images. Original magnification: 10×. (b) Measured pH of culture media after 24 h incubation with HUVECs. Blank indicates media without cells. EGM-2 indicates non-adjusted media. (c) HUVEC adhesion density on culture plates. EGM-2 (t = 0) represents HUVEC adhesion density after 24 h pre-incubation for cell stabilization prior to incubation with the alkaline media. (d) F-actin area per adhered HUVEC nucleus. (e) Cell diameter aspect ratio (D_{max}/D_{min}). Values in (b) are mean ± SD, and (c) – (e) are mean ± standard error of the means; n = 3 for all measurements; $^{*}p < 0.05$.

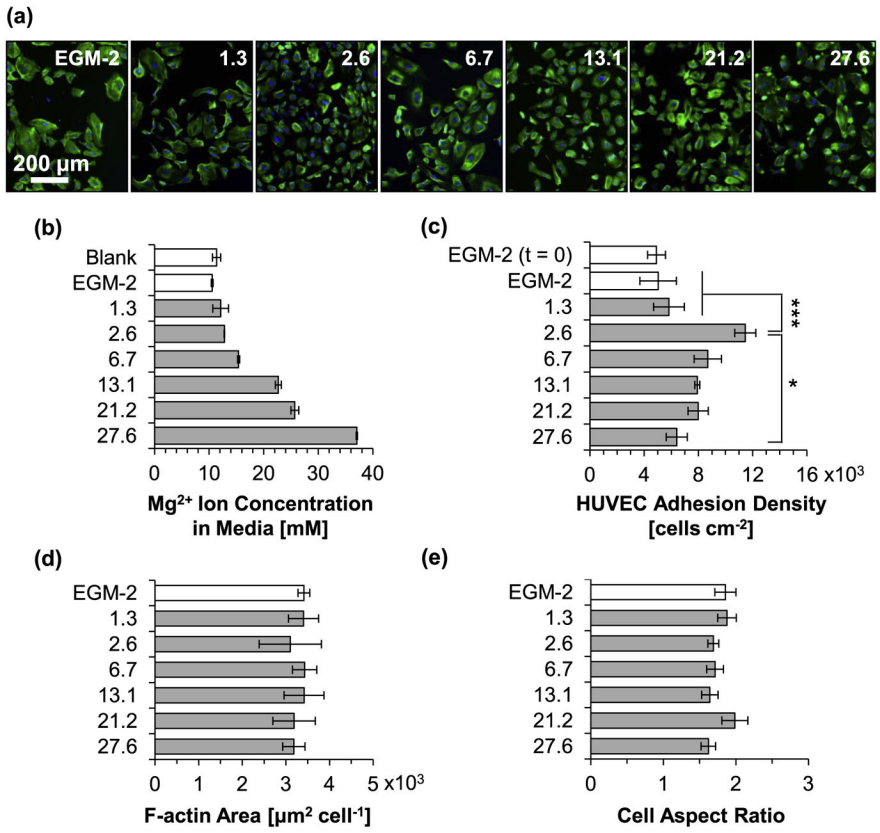

Fig. 14.

HUVEC behaviors after 24 h of incubation in complete EGM™-2 media supplemented with Mg^{2+} concentration of 0–27.6 mM initially. (a) Fluorescence images of HUVECs. Blue color indicates DAPI stained nuclei and green color indicates Alexa Fluor® 488 stained F-actin (cytoskeleton). Scale bar = 200 μm for all images. Original magnification: 10×. (b) Measured Mg^{2+} ion concentration in culture media after 24 h of incubation with HUVECs. Blank indicates media without cells. EGM-2 indicates non-adjusted media. (c) HUVEC adhesion density on culture plates. EGM-2 (t = 0) represents HUVEC adhesion density after 24 h pre-incubation for cell stabilization prior to incubation with the adjusted media. (d) F-actin area per adhered HUVEC nucleus. (e) Cell diameter aspect ratio (D_{max}/D_{min}). Values in (b) are mean ± SD, and (c) – (e) are mean ± standard error of the means; n = 3 for all measurements; $^{*}p < 0.05$, $^{***}p < 0.001$.

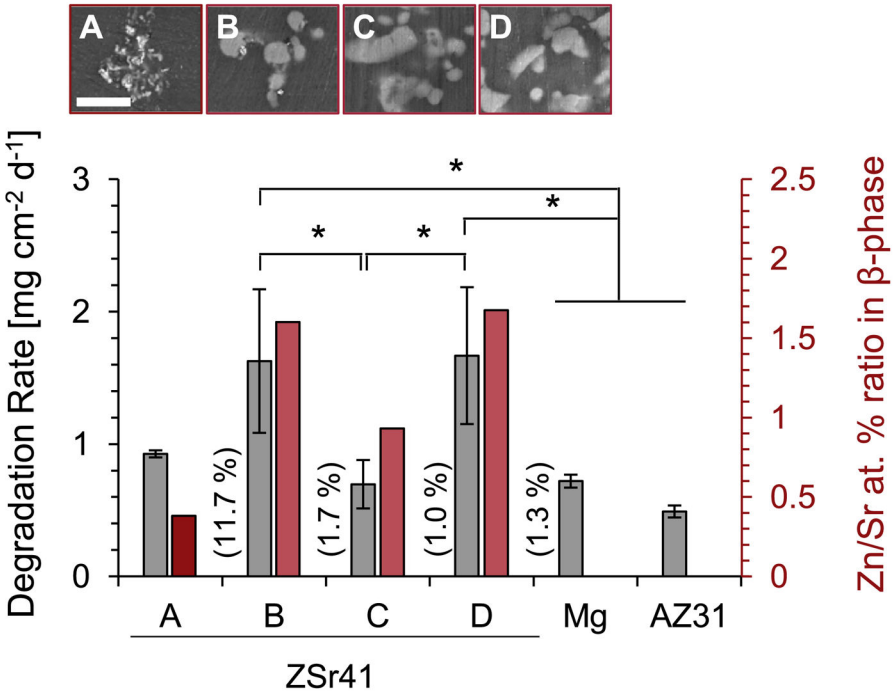

Fig. 15.

Summary of the average daily degradation rate (mass loss rate) per unit surface area in EGM™-2 media of the Mg-based materials in this study and critical Zn/Sr at% ratios that affect β-phase formation and corrosion resistance of ZSr41 alloys. Scale bar in SEM micrographs = 10 μm. Numbers in parenthesis indicate elemental O content (at%) in the β-phase of each ZSr41 alloy. Degradation values are mean ± SD, n = 3; $^{*}p < 0.05$.

Table 1

Quantification of surface elemental composition (at%) from EDS analysis of points 1, 3, 5, and 7 (i.e., intermetallic phases in ZSr41A-D, respectively) and corresponding Zn/Sr at% ratio.

Point (Alloy)	Mg	C	O	Zn	Sr	Ca	Zn/Sr
1 (ZSr41A)	59.9	22.8	11.7	1.4	3.6	0.6	0.4
3 (ZSr41B)	70.7	15.3	1.7	7.5	4.7	0.1	1.6
5 (ZSr41C)	75.1	15.4	1.0	4.1	4.4	0.1	0.9
7 (ZSr41D)	70.2	18.0	1.3	6.5	3.9	0.1	1.7

Table 2

Timeline of the development of as-cast crystalline Mg-Zn-Sr ternary alloys up-to-date. Remarks summarize the key information of interest from the reported literature. Note: “Alloy design” articles typically included microstructure, crystallinity, and/or results on mechanical properties. “Bio-corrosion/Corrosion” articles typically included alloy design, and electrochemical/immersion results; and “Cell Studies” articles typically included alloy design, bio-corrosion, and cell culture results. Values obtained from Refs. [26–28,52–56,67].

Year	Ref	Zn Content (wt%)	Sr Content (wt%)	Zn/Sr at% ratio	Type of Article	*In vitro* cellular assays	Remarks
2007	[54]	All	All	All	Alloy design	–	First to provide a thermodynamic assessment and phase diagram
2012	[52]	2	0.5	5.36	Bio-Corrosion	–	First to systematically assess the bio-corrosion properties *in vitro* (Hank’s solution for 8 days)
		4	0.5	10.72			
		6	0.5	16.08			
2013	[26]	4	1	5.36	Bio-Corrosion	–	First to report bio-corrosion properties *in vitro* in simulated body fluid (SBF for 15 days)
2013	[55]	4	0.5	10.72	Bio-	–	First to report systematic evaluation of bio-corrosion properties in vitro in simulated body fluid (SBF for 17 days)
		4	1.5	3.57	Corrosion		
2013	[27]	4	0.15	35.74	Cell Studies	Cytocompatibility	First to evaluate Mg-Zn-Sr alloy cytocompatibility which was evaluated using the direct culture with human embryonic stem cells
		4	0.5	10.72			
		4	1	5.36			
		4	1.5	3.57			
2014	[53]	1	0.2	6.70	Cell Studies	Cytocompatibility	First to process alloys via zone purification and backward extrusion. Cytocompatibility was assessed using the extract-based method with L929 fibroblasts
		1	0.5	2.68			
		1	0.8	1.68			
		1	1	1.34			
2014	[56]	0.4	0.05	10.72	Corrosion	–	First to provide optimization of alloy corrosion resistance for structural applications
		1	0.05	26.80			
		1	0.1	13.40			
2014	[67]	N/A	N/A	N/A	Cell Studies	Cytocompatibility Hemocompatibility Anti-bacterial	First to evaluate alloy hemocompatibility and *anti*-bacterial efficacy
2015	[28]	4	0.15	35.74	Cell Studies	Cytocompatibility Hemocompatibility	First to evaluate and compare alloy degradation in whole blood vs. plasma fraction of blood
		4	0.5	10.72			
		4	1	5.36			

Year	Ref	Zn Content (wt%)	Sr Content (wt%)	Zn/Sr at% ratio	Type of Article	*In vitro* cellular assays	Remarks
		4	1.5	3.57			
2015	Present Study	4	0.15	35.74	Cell Studies	Cytocompatibility Inflammatory response	First to evaluate cytocompatibility with HUVECs in the direct culture and in vitro inflammatory response via VCAM-1 expression
		4	0.5	10.72			
		4	1	5.36			
		4	1.5	3.57			

Table 3

Ionic concentrations (mM) from inorganic salts in MCDB 131 (non-commercial analog of EGM™-2), mTeSR®1, and r-SBF in comparison with human blood plasma. Compiled from Refs. [45,47,51,70].

	MCDB 131	mTeSR®1	r-SBF	Plasma
Na^+	124.5	113.74	142	142
K^+	4	3.26	5	5
Mg^{2+}	10	0.56	1.5	1.5
Li^{2+}	–	0.98	–	–
Ca^{2+}	1.6	0.82	2.5	2.5
Fe^{3+}	0.001	–	–	–
Cl^-	117.2	100.96	103	103
HCO_3^-	14	18	27	27
$H_2PO_4^-$	0.5	0.36	–	–
HPO_4^{2-}	–	0.39	1	1
SO_4^{2-}	10	0.32	0.5	0.5
Ionic Strength	0.173	0.123	0.150	0.150
Osmolality (mOsm/kg H_2O)[a]	260–290[b]	330–350[c]		290

[a] Osmolality values reported with the presence of organic species and buffers.

[b] Osmolality for EGM™-2 media from technical specification sheet. Lonza Cat# CC-3162.

[c] Osmolality for mTeSR®1 media from technical specification sheet. Stem Cell Tech, Cat# 85850.